A Month of Monitoring the New Magnetar Swift J1555.2−5402 during an X-Ray Outburst

Teruaki Enoto[1] , Mason Ng[2] , Chin-Ping Hu[3] , Tolga Güver[4,5] , Gaurava K. Jaisawal[6] , Brendan O'Connor[7,8,9,10] , Ersin Göğüş[11] , Amy Lien[12,13,14] , Shota Kisaka[15] , Zorawar Wadiasingh[10,16] , Walid A. Majid[17,18] , Aaron B. Pearlman[18,19,20,31,32] , Zaven Arzoumanian[10] , Karishma Bansal[17] , Harsha Blumer[21,22] , Deepto Chakrabarty[2] , Keith Gendreau[10] , Wynn C. G. Ho[23] , Chryssa Kouveliotou[7,8] , Paul S. Ray[24] , Tod E. Strohmayer[25] , George Younes[7,8] , David M. Palmer[26] , Takanori Sakamoto[27] , Takuya Akahori[28,29] , and Sujin Eie[28,30]

[1] RIKEN Cluster for Pioneering Research, 2-1 Hirosawa, Wako, Saitama 351-0198, Japan
[2] MIT Kavli Institute for Astrophysics and Space Research, Massachusetts Institute of Technology, Cambridge, MA 02139, USA
[3] Department of Physics, National Changhua University of Education, Changhua 50007, Taiwan
[4] Istanbul University, Science Faculty, Department of Astronomy and Space Sciences, Beyazıt, 34119, İstanbul, Turkey
[5] Istanbul University Observatory Research and Application Center, Istanbul University 34119, İstanbul, Turkey
[6] National Space Institute, Technical University of Denmark, Elektrovej 327-328, DK-2800 Lyngby, Denmark
[7] Department of Physics, The George Washington University, 725 21st Street NW, Washington, DC 20052, USA
[8] Astronomy, Physics and Statistics Institute of Sciences (APSIS), The George Washington University, Washington, DC 20052, USA
[9] Department of Astronomy, University of Maryland, College Park, MD 20742-4111, USA
[10] Astrophysics Science Division, NASA Goddard Space Flight Center, Greenbelt, MD 20771, USA
[11] Sabancı University, Faculty of Engineering and Natural Sciences, İstanbul 34956, Turkey
[12] Center for Research and Exploration in Space Science and Technology (CRESST) and NASA Goddard Space Flight Center, Greenbelt, MD 20771, USA
[13] Department of Physics, University of Maryland, Baltimore County, 1000 Hilltop Circle, Baltimore, MD 21250, USA
[14] University of Tampa, Department of Chemistry, Biochemistry, and Physics, 401 West Kennedy Boulevard, Tampa, FL 33606, USA
[15] Department of Physics, Hiroshima University, Higashi-Hiroshima, 739-8526, Japan
[16] Universities Space Research Association (USRA) Columbia, MD 21046, USA
[17] Jet Propulsion Laboratory, California Institute of Technology, Pasadena, CA 91109, USA
[18] Division of Physics, Mathematics, and Astronomy, California Institute of Technology, Pasadena, CA 91125, USA
[19] Department of Physics, McGill University, 3600 rue University, Montréal, QC H3A 2T8, Canada
[20] McGill Space Institute, McGill University, 3550 rue University, Montréal, QC H3A 2A7, Canada
[21] Department of Physics and Astronomy, West Virginia University, Morgantown, WV 26506, USA
[22] Center for Gravitational Waves and Cosmology, West Virginia University, Chestnut Ridge Research Building, Morgantown, WV 26505, USA
[23] Department of Physics and Astronomy, Haverford College, 370 Lancaster Avenue, Haverford, PA 19041, USA
[24] Space Science Division, U.S. Naval Research Laboratory, Washington, DC 20375, USA
[25] Astrophysics Science Division and Joint Space-Science Institute, NASA's Goddard Space Flight Center, Greenbelt, MD 20771, USA
[26] Los Alamos National Laboratory, Los Alamos, NM 87545, USA
[27] College of Science and Engineering, Department of Physical Sciences, Aoyama Gakuin University, 5-10-1 Fuchinobe, Chuo-ku, Sagamihara-shi Kanagawa 252-5258, Japan
[28] Mizusawa VLBI Observatory, National Astronomical Observatory of Japan, 2-21-1, Osawa, Mitaka, Tokyo 181-8588, Japan
[29] Operation Division, Square Kilometre Array Observatory, Jodrel Bank Observatory, Lower Withington, Macclesfield, Cheshire SK11 9FT, UK
[30] Department of Astronomy, Graduate School of Science, The University of Tokyo, 7-3-1 Hongo, Bunkyo-ku, Tokyo 113-0033, Japan

Abstract

The soft gamma-ray repeater Swift J1555.2−5402 was discovered by means of a short burst detected with Swift BAT on 2021 June 3. Then, 1.6 hr after the burst, the Neutron star Interior Composition Explorer (NICER) started daily monitoring of this target for a month. The absorbed 2–10 keV flux stayed nearly constant at around 4×10^{-11} erg s^{-1} cm^{-2} during the monitoring, showing only a slight gradual decline. An absorbed blackbody with a temperature of 1.1 keV approximates the soft X-ray spectrum. A 3.86 s periodicity is detected, and the period derivative is measured to be $3.05(7) \times 10^{-11}$ s s^{-1}. The soft X-ray pulse shows a single sinusoidal shape with an rms pulsed fraction that increases as a function of energy from 15% at 1.5 keV to 39% at 7 keV. The equatorial surface magnetic field, characteristic age, and spin-down luminosity are derived under the dipole field approximation to be 3.5×10^{14} G, 2.0 kyr, and 2.1×10^{34} erg s^{-1}, respectively. We detect 5 and 45 bursts with Swift/BAT and NICER, respectively. Based on these properties, this new source is classified as a magnetar. A hard X-ray power-law component that extends up to at least 40 keV is detected with the Nuclear Spectroscopic Telescope Array (NuSTAR). The 10–60 keV flux is $\sim 9 \times 10^{-12}$ erg s^{-1} cm^{-2} with a photon index of ~ 1.2. The pulsed fraction has a sharp cutoff at around 10 keV with an upper limit ($\lesssim 10\%$) in the hard-tail band. No radio pulsations are detected during the DSN or VERA observations. The 7σ upper limits of the flux density are 0.043 and 0.026 mJy at the S and X bands, respectively.

1. Introduction

Magnetars are highly magnetized neutron stars that are usually bright in X-rays as a result of the release of an

---

[31] McGill Space Institute (MSI) Fellow.
[32] FRQNT Postdoctoral Fellow.

enormous amount of magnetic energy stored in the stellar interior and the magnetosphere (Mereghetti 2008; Kaspi & Beloborodov 2017). Among them, sources emitting repetitive soft gamma-ray bursts are historically called soft gamma-ray repeaters (SGRs; e.g., Kouveliotou et al. 1998). In the last decade, systematic monitoring of magnetars in X-rays, mainly with the X-Ray Telescope (XRT) on board the Neil Gehrels Swift Observatory, revealed that many transient magnetars spend most of their time in a quiescent state with low activity. However, they occasionally exhibit a sudden X-ray brightening, where the X-ray flux reaches an initial plateau of 10^{-11}–10^{-10} erg s^{-1} cm^{-2} lasting a few weeks, followed by a gradual decay over a variety of timescales (Enoto et al. 2017; Coti Zelati et al. 2018). These magnetar outbursts are characterized by enhanced persistent X-ray emission, sporadic short bursts, pulsar timing anomalies, and, rarely, giant flares. Their origin has been attributed to various mechanisms, such as the relaxation process of twisted magnetic fields, starquakes, magnetothermal evolution, and magnetic field dissipation (Thompson & Duncan 1995, 1996; Perna & Pons 2011; Beloborodov & Li 2016). Multiwavelength observations of these outbursts are essential to address a wide range of astronomical topics, as demonstrated, for example, with the discovery of fast radio bursts (FRBs) associated with a short hard X-ray burst from the Galactic magnetar SGR J1935+2154 in 2020 (Bochenek et al. 2020; CHIME/FRB Collaboration et al. 2020; Mereghetti et al. 2020; Li et al. 2021; Ridnaia et al. 2021; Tavani et al. 2021). Such a connection between magnetars and FRBs is also supported by the indication that extragalactic FRBs have the statistical signatures of magnetar short bursts (e.g., Wadiasingh & Timokhin 2019).

On 2021 June 3, a new SGR, Swift J1555.2−5402, was discovered through a short burst detection with the Burst Alert Telescope (BAT) on board Swift (Palmer et al. 2021). Immediately after the notification of the burst from this source, several X-ray satellites started follow-up observations of this magnetar candidate. These observations were promptly used to measure the spin frequency and frequency derivative (Israel et al. 2021; Ng et al. 2021; Coti Zelati et al. 2021b) and detected several short bursts (Palmer 2021). Based on the measured timing parameters and distinctive magnetar characteristics, this new source was classified as a magnetar. In addition, several radio telescopes searched for radio emission and pulsations (Bansal et al. 2021; Burgay et al. 2021; Singh & Roy 2021). In this Letter, we report on the X-ray temporal and spectral characteristics of this new magnetar observed with Swift, the Neutron star Interior Composition Explorer (NICER), and the Nuclear Spectroscopic Telescope Array (NuSTAR) during the initial 29 days of its X-ray outburst; our observations were also coordinated with radio monitoring.

The celestial position of Swift J1555.2−5402 is close to another magnetar, 1E 1547.0−5408, with an angular separation of about $0°.7$. The distance to 1E 1547.0−5408 is estimated to be 4–4.5 kpc from a dust-scattering halo (Tiengo et al. 2010) and a possible association with SNR G327.24−0.13 (Gelfand & Gaensler 2007). By contrast, no definitive information is available about the distance to Swift J1555.2−5402 (Section 3.5). Taking into account the fact that the column density of Swift J1555.2−5402 ($N_H = 8.7 \times 10^{22}$ cm^{-2}) is larger than that of 1E 1547.0−5408 ($N_H = 3.2 \times 10^{22}$ cm^{-2}; Enoto et al. 2010b), we assume a fiducial distance d of 10 kpc and the normalization factor $d_{10} = d/(10$ kpc) throughout this

Letter. This distance corresponds to a location on the Scutum–Centaurus Arm.

2. Observation and Data Reduction

2.1. Swift

The Swift BAT (Gehrels et al. 2004) detected a burst from an unknown source at 09:45:46 UT on 2021 June 3 (trigger number 1053220) and immediately pointed to the source direction (Palmer et al. 2021). The Swift XRT (Burrows et al. 2005) obtained X-ray data in the WT mode for 62 s from 97 s after the BAT trigger and then in the PC mode for ∼1.7 ks from 1.1 hr after the burst. The XRT observations determined the source position (J2000.0) to be R.A. $=15^h 55^m 08^s.66$ and decl. $= -54° 03' 41''.1$ with an uncertainty radius of $2''.2$ at a 90% confidence level (Evans 2021). We adopt this source position for all analyses in this Letter. The BAT detected another four short bursts from the same direction, as summarized in Appendix Table B1. We analyzed the BAT data using the standard HEASoft BAT pipelines (version 6.28), following the same procedure described in Lien et al. (2016); these results are presented in Section 3.3.

We analyzed the XRT data obtained on June 3, 4, 5, and 7. The observation IDs (ObsIDs) used in this Letter are listed in Appendix Table A1. The observations on June 4, 5, and 7 were carried out in the WT mode for a total of 8.9 ks. We processed the data through the standard procedure of FTOOLS `xrtpipeline` with the default filtering criteria. For PC mode data, we extracted source photons from a circular region with a 20 pixel radius (1 pixel $= 2''.36$) centered at the target, whereas we collected background spectra from a source-free region with a similar (20 pixel) radius located far ($>2'$) from the source. For the one-dimensional WT mode data, we extracted the source spectra from a rectangular strip of length 40 pixels (∼94''). The background was estimated using a source-free region of a similar size located ∼2' from the source position. We used the latest available RMF file in CALDB version 20210504 and generated the ARF files with the `xrtmkarf` tool.

2.2. NICER

NICER (Gendreau et al. 2016), on board the International Space Station, began X-ray observations of the source at 11:21:31 UT on 2021 June 3, 1.6 hr after the first short burst detected with Swift BAT. This initial NICER observation was 2.4 ks long in exposure (ObsID 4202190101), and it was followed by high-cadence monitoring (see Appendix Table A2) carried out almost daily for 29 days under an approved Cycle 3 proposal. Each ObsID had roughly 2 ks exposure and was divided into several continuous good time intervals (GTIs) with exposures of a few hundred seconds for each.

The NICER's X-ray Timing Instrument (XTI) has 52 on-orbit active modules, each of which consists of coaligned X-ray concentrators and silicon drift detectors. The XTI has a time resolution of <100 ns, and the total effective area is about 1,800 cm^2 at around 1.5 keV. We performed the standard analysis procedures using `NICERDAS` (version 2020-04-23_V007a) in HEASoft 6.27.2 and the NICER calibration database (version 20200722). We generated level 2 cleaned events with the `nicerl2` command. For the barycentric correction, we used `barycorr` with Jet Propulsion Laboratory solar system development ephemeris DE405 for the source

coordinates stated above (Standish 1998). For timing analyses and burst searches, we utilized all 52 active modules. For spectral studies, we further excluded module numbers 14 and 34 to avoid potential contamination by instrumental noise in the soft energy band. The background spectral model is generated using the 3C50 background model with the `nibackgen3c50` command (Remillard et al. 2021).[33]

2.3. NuSTAR

NuSTAR (Harrison et al. 2013) observed Swift J1555.2−5402 on June 5–6 for a 38.4 ks exposure and two additional contemporaneous observations with NICER on June 9 (25 ks) and 21 (29 ks). We processed and filtered the NuSTAR data following the standard procedures with HEASoft version 6.28 and CALDB version 20210524 using the `nupipline` and `nuproducts` commands. We extracted on-source and background spectra from circular regions of 80″ radius centered at the source position and in a source-free region, respectively. The background-subtracted source count rate of FPMA was about 1 count s^{-1} in the 3–79 keV band. For the spectral fitting, we grouped source spectra using the `grppha` tool of HEASoft, such that each spectral bin would have a minimum of 50 counts.

2.4. Deep Space Network

We carried out radio observations of Swift J1555.2−5402 for a total exposure of roughly 10.8 hr at five epochs during 2021 June 4–12 using different Deep Space Network (DSN) radio telescopes (see Table A4). Simultaneous dual-frequency bands, with center frequencies at 2.2 (*S* band) and 8.4 (*X* band) GHz, were used for all observations. We used a single circular polarization mode for DSS-34 and DSS-36, whereas a dual circular polarization mode was used at each frequency band for DSS-43.

We recorded the data in filter-bank mode with a time resolution of 512 μs and frequency resolution of 1 MHz using the pulsar machine in Canberra. The data processing procedure follows similar steps to those presented in earlier studies of pulsars and magnetars with the DSN (e.g., Majid et al. 2017; Pearlman et al. 2018, 2019). After first flattening the bandpass response in each data set, we removed the low-frequency variations in the temporal baseline of each frequency channel by subtracting the moving average from each data point with a time constant of 10 s. The sample times were then corrected to the solar system barycenter.

2.5. VERA (K Band)

The 20 m diameter Ishigaki-jima station of the VLBI Exploration of Radio Astrometry (VERA) conducted a target-of-opportunity observation of this source at an observation frequency of 22 GHz (1.3 cm, *K* band) with a bandwidth of 512 MHz. The acquired data for 1 hr at 14:40–15:40 UT on 2021 June 6 were processed and folded to explore radio pulsations both with and without assuming the rotation period. Because the data quality was limited due to a low elevation of the object and bad weather conditions, we could only set an upper limit of the peak flux density of 1.02 Jy (1σ).

3. Analysis and Results

3.1. X-Ray Timing Analyses

Figure 1 shows the time series of the physical parameters of Swift J1555.2−5402 during NICER monitoring for the 29 days from shortly after the onset of the outburst until July 1. In constructing the time series, we first derived the pulsar spin ephemeris, for which we used a Gaussian pulse template and constructed pulse times of arrival (TOAs) with an integration time of 300 s and a minimum exposure of 200 s contained in each bin, using the script `photon_toa.py` from NICER-soft.[34] The timing analysis was carried out over 2–8 keV, where the energy range was determined from a Z_n^2 search with $n = 2$ to optimize the pulse significance (Buccheri et al. 1983). We used the Python-based package for high-precision timing analysis "PINT" (Luo et al. 2021; version 0.8.2) to compute the best timing model through a weighted least-squares fit to the TOAs. The TOAs were found to be well described by a fifth-order polynomial model, as summarized in Table 1, for the spin evolution of Swift J1555.2−5402. The best-fit frequency and its derivatives are $\nu = 0.258997103(8)$ Hz, $\dot{\nu} = -2.04(5) \times 10^{-12}$ Hz s^{-1}, $\ddot{\nu} = -4.50(13) \times 10^{-18}$ Hz s^{-2}, $\nu^{(3)} = -1.10(10) \times 10^{-23}$ Hz s^{-3}, $\nu^{(4)} = 3.59(15) \times 10^{-29}$ Hz s^{-4}, and $\nu^{(5)} = 1.59(14) \times 10^{-34}$ Hz s^{-5} at barycentric epoch $T_0 =$ MJD 59,382.7549. NICER's sensitivity enables our measurement up to fifth order in frequency with TOAs of only 300 s.

In Figures 2(a)–(d), we present the energy-resolved and background-subtracted pulse profiles of Swift J1555.2−5402 in the 2–3 and 3–8 keV bands with NICER and 3–8, 8–12, and 12–20 keV with NuSTAR, where estimates of the background rates were made with the `nibackgen3C50` tool for the NICER data and based on the measured rate in the background region for the NuSTAR data. The soft X-ray profile (2–12 keV) shows a single-peaked, nearly sinusoidal shape, while the pulsation in the hard X-ray band ($\gtrsim$12 keV) was not detected. We further divided the data into finer energy bands and calculated, in Figure 2(f), the time-averaged rms pulsed fraction (PF) as defined in Bildsten et al. (1997) and Woods et al. (2004). Both the NICER and NuSTAR observations suggest that the rms PF increases from ∼30% in the softer band (3–4 keV) to a maximum of ∼40% at around 7 keV and then decreases with energy to $\lesssim$10%. We also found that the PF in the 3–8 keV range remained almost constant during the observed period (Figure 1(e)).

3.2. X-Ray Spectral Analyses

The right panels of Figure 1 show the long-term spectral properties of Swift J1555.2−5402 obtained with Swift, NICER, and NuSTAR data. Here we applied a single-temperature blackbody multiplied by the Tuebingen–Boulder interstellar absorption model (`tbabs*bbodyrad` in Xspec terminology) to derive the physical parameters at each epoch (Wilms et al. 2000). The first data point in each of the right panels corresponds to the initial 1.7 ks Swift PC spectrum obtained ∼1.1 hr after the BAT trigger, which is well fitted with the model above (χ^2 of 113 for 128 degrees of freedom, dof). We derived a best-fit hydrogen column density of $N_H = 6.8^{+2.0}_{-1.7} \times 10^{22}$ cm^{-2} and blackbody temperature of $kT = 1.26^{+0.20}_{-0.16}$ keV. The absorbed 2–10 keV flux is $6.8^{+0.9}_{-0.8} \times 10^{-11}$ erg s^{-1} cm^{-2}. This flux is significantly higher than those in the following observations with the Swift/XRT in the WT mode and NICER monitoring.
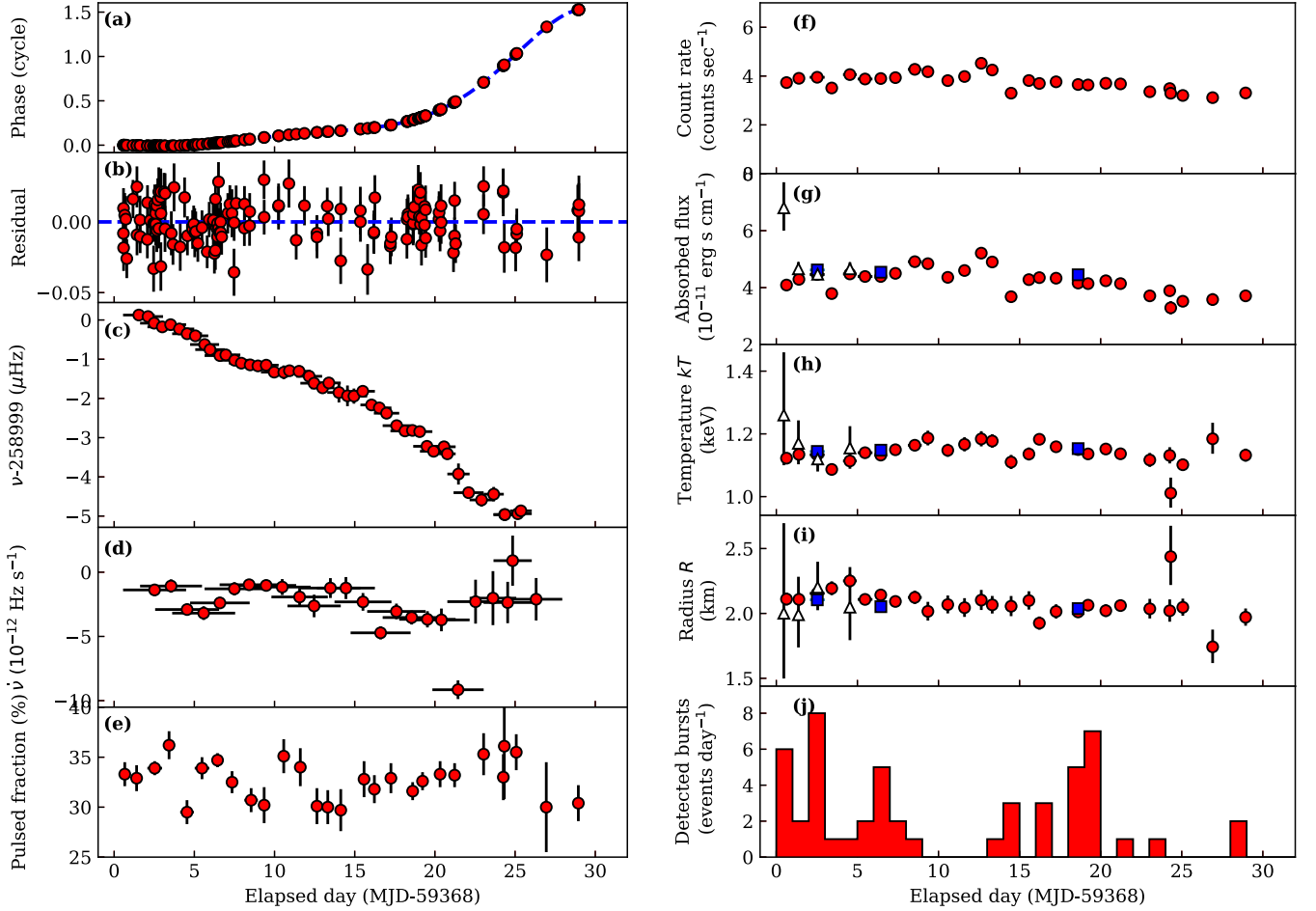

Figure 1. NICER monitoring of the timing (left panels) and spectral evolution (right panels) of the 2021 outburst of Swift J1555.2−5402 over 29 days (2021 June 3–July 1; MJD 59,368–59,396). The time origin MJD 59,368 is the day when the first burst was detected with Swift/BAT. (a) Intrinsic pulse-phase evolution with respect to a folding frequency of $\nu_{\rm fold} = 0.258997274$ Hz and a folding frequency derivative of $\dot{\nu}_{\rm fold} = -1.63 \times 10^{-12}$ Hz s^{-1}; the dashed line is the best-fit model with a fifth-order polynomial. (b) Phase residuals (cycles) after correcting for the spin derivatives (up to fifth order). (c) Spin frequency with 2 day windows in steps of 0.5 day. (d) Spin frequency derivative with 4 day windows in steps of 1 day. (e) The rms PF in the 3–8 keV band. (f) Background-subtracted 2–10 keV NICER count rate. (g) The 2–10 keV absorbed X-ray flux obtained with Swift (open triangles), NICER only (red circles), and NICER simultaneously fitted with NuSTAR (blue squares). The symbols are the same in panels (h) and (i). (h) Blackbody temperature (keV). (i) Emission radius of the blackbody component assuming a fiducial distance of 10 kpc. (j) Number of short bursts per day detected with NICER and Swift/BAT. Error bars are at a 68% confidence limit in these plots.

The subsequent daily NICER spectra (1.7–10 keV) were systematically fitted with the same model with the hydrogen column density tied to be the same value among all NICER spectra at $N_{\rm H} = (8.88 \pm 0.12) \times 10^{22}$ cm^{-2}. Each observation has $\sim$4 counts s^{-1} (Figure 1(f)). The reduced χ^2 values were $\sim$0.9–1.2 for $\sim$100–400 dof. No spectral variation during the initial monitoring was found. The absorbed and unabsorbed 2–10 keV fluxes were $\sim 4.3 \times 10^{-11}$ (Figure 1(g)) and $\sim 7.5 \times 10^{-11}$ erg s^{-1} cm^{-2}, respectively. The derived temperature and emission radius were constant at $\sim$1.1 keV (Figure 1(h)) and $\sim 2\,d_{10}$ km (Figure 1(i)), respectively (Section 3.5). These NICER parameters are consistent with those obtained with the WT mode data of Swift/XRT.

We performed joint spectral fits of three observations of NICER and NuSTAR on June 5–6, 9, and 21. Since the NICER spectra showed no significant time variation, we extracted the NICER spectra for the period on the same day as NuSTAR and regarded them as simultaneous, even if their observation periods were not fully simultaneous. The column densities among the three epochs are tied to the same value. The best-fit spectral model is shown in Figure 3. In addition to the soft X-ray blackbody component, a hard X-ray component above 10 keV

was detected with 3σ significance extending up to at least 40 keV. The hard X-ray flux, when fitted by the power-law model, was $(7-9) \times 10^{-12}$ erg s^{-1} cm^{-2} in the 10–60 keV band with a power-law photon index of 1.2–1.7. We also performed a combined fit of all three epochs, given that no significant spectral change was observed between them. The resultant average νF_ν is shown in the right panel of Figure 3 and Table 1. The νF_ν plot shows that the hard X-ray component above 10 keV exceeds the high-energy tail of the soft blackbody component.

3.3. Short Burst Analyses

Swift BAT detected five short bursts, as summarized in Appendix Table B1. For the first detected burst on June 3 (an onboard trigger), we used the data from $T-240$ to $T+100$ s, where T is the burst detection time, whereas we used the $\sim$3 s interval events collected through subthreshold triggers[35] in our analyses of the other bursts. The BAT event data have a time

---

[35] These are also called failed triggers, which are detections that pass the rate trigger criteria but fail the image detection threshold.

Table 1
Summary of the Timing and Spectral Properties of Swift J1555.2−5402

Parameter	Values			
Timing Properties (NICER Monitoring)				
MJD range				59,368.58–59,396.98
Epoch T_0 (MJD)				59,382.7549
Spin frequency ν (Hz)				0.258997103(8)
Frequency derivative $\dot{\nu}$ (10^{-12} Hz s^{-1})				−2.04(5)
Second frequency derivative $\ddot{\nu}$ (10^{-18} Hz s^{-2})				−4.50(13)
Third frequency derivative $\nu^{(3)}$ (10^{-23} Hz s^{-3})				−1.10(10)
Fourth frequency derivative $\nu^{(4)}$ (10^{-29} Hz s^{-4})				3.59(15)
Fifth frequency derivative $\nu^{(5)}$ (10^{-34} Hz s^{-5})				1.59(14)
rms residual (phase)				0.014
χ^2/dof				117.863/126
Period P (s)				3.86104705(12)
Period derivative $\dot{P}$ (10^{-11} s s^{-1})				3.05(7)
Second period derivative $\ddot{P}$ (10^{-17} s s^{-2})				6.7(2)
Third period derivative $P^{(3)}$ (10^{-22} s s^{-3})				1.63(15)
Fourth period derivative $P^{(4)}$ (10^{-28} s s^{-4})				−5.3(2)
Fifth period derivative $P^{(5)}$ (10^{-33} s s^{-5})				−2.4(2)
Characteristic age τ_c (kyr)				2.01(5)
Surface magnetic field B_{surf} (10^{14} G)				3.47(4)
Spin-down luminosity L_{sd} (10^{34} erg s^{-1})				2.09(5)
Spectral Properties (NICER+NuSTAR Joint Fit)				
Joint observation numbers	1	2	3	Average
Observation date (MJD)	59,370	59,374	59,386	⋯
Column density N_H (10^{22} cm^{-2})		8.72(8)		8.69(7)
Temperature kT (keV)	1.144(4)	1.148(4)	1.153(4)	1.149(3)
Radius R (km)	2.10(2)	2.05(2)	2.04(2)	2.06(3)
Photon index Γ	1.27(12)	1.68(17)	1.15(0.16)	1.35(9)
Absorbed 2–10 keV flux (10^{-12} erg s^{-1} cm^{-2})	$46.16^{+0.19}_{-0.38}$	$45.41^{+0.14}_{-0.55}$	$44.48^{+0.18}_{-0.45}$	$45.81^{+0.04}_{-0.19}$
Unabsorbed 2–10 keV flux (10^{-12} erg s^{-1} cm^{-2})	70.60(32)	69.39(35)	67.80(36)	69.5(4)
10–60 keV flux (10^{-12} erg s^{-1} cm^{-2})	9.32 ± 0.34	7.73 ± 0.35	8.72 ± 0.85	9.02 ± 0.24
2–10 keV luminosity L_x (10^{35} erg s^{-1})	8.45	8.30	8.11	8.32
10–60 keV luminosity L_x (10^{35} erg s^{-1})	1.11	0.93	1.04	1.08
Quiescent (Swift)				
Absorbed 2–10 keV flux (10^{-12} erg s^{-1} cm^{-2})		<0.26 (3σ)		
Unabsorbed 2–10 keV flux (10^{-12} erg s^{-1} cm^{-2})		<1.2 (3σ)		
2–10 keV luminosity L_x (10^{35} erg s^{-1})		<0.15 (3σ)		

Note. The column density of the three joint NICER and NuSTAR spectral fittings is fixed to the same value. The X-ray luminosity and radius are calculated on an assumption of a fiducial distance of 10 kpc. Quoted errors indicate the 68% confidence limit. The quiescent X-ray upper limits are derived with an assumed temperature of 0.45 keV (see the text).

resolution of ∼100 μs (Barthelmy et al. 2005). The BAT temporal analysis utilizes light curves binned in 1, 2, and 4 ms. Our BAT spectral analysis was performed using spectra created with the T_{90} duration of each burst, which is the duration that covers 90% of the burst emission. All of the spectra were successfully fitted with a single blackbody model (`bbodyrad` model in `Xspec`), except for the one on June 7, the statistics of which were too poor to give meaningful constraints.

We also searched the 2–8 keV NICER event data for short bursts using the Bayesian block technique[36] (Scargle et al. 2013) and the data filtering criteria in Appendix B. The blocks with high backgrounds and durations longer than ∼1 s are further filtered out on the basis of comparison between the housekeeping data (`mkf` files), multiple blocks in one burst, and blocks close to the GTI boundaries. We used the Poisson probability to

determine the significance of detecting a number of photons in a block, where the nonburst count rate was calculated from 1 s intervals close in time to the bursts. We identified 45 short bursts exceeding a 5σ detection significance, as summarized in Appendix Table B2. The average duration of the bursts was 23 ± 17 ms, and 13 photons were detected in a burst, on average. Note that burst 27–1 on the list occurred during the tail of burst 27, and we included it in burst 27 in the calculation.

We stacked the detected bursts to obtain an average spectrum and found it to be equally well fitted with both a single blackbody (`tbabs ∗ bbodyrad`) and a power-law (`tbabs ∗ pegpwrlw`) with Cash statistics of C-stat $= 261.1$ and 264.0, respectively, with 310 dof. When fixing the absorption column density at $N_H = 8.72 \times 10^{22}$ cm^{-2} (Table 1), the former model gave a blackbody temperature of $2.9^{+0.8}_{-0.5}$ keV, whereas the latter gave a photon index of 0.0 ± 0.2. Using the blackbody model, we find an average unabsorbed flux of $(1.3 \pm 0.1) \times 10^{-8}$ erg s^{-1} cm^{-2} in the

---

[36] https://docs.astropy.org/en/stable/api/astropy.stats.bayesian_blocks.html
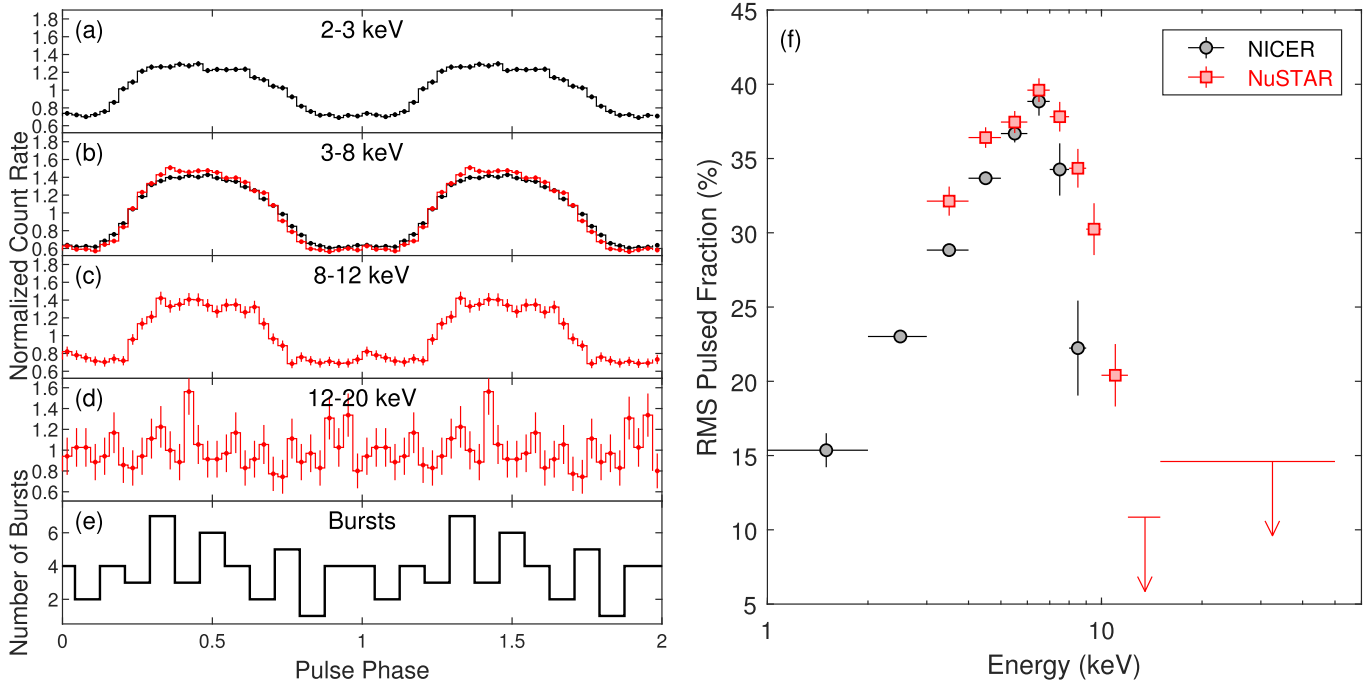
Figure 2. Panels (a)–(d) are background-subtracted X-ray pulse profiles of Swift J1555.2−5402 in the 2–3, 3–8, 8–12, and 12–20 keV bands, respectively, taken with (black) NICER and (red) NuSTAR. The amplitudes are normalized relative to the mean count rate. Two cycles are shown in this figure for clarity. Error bars indicate 1σ uncertainties. Panel (e) shows the phase distribution of short bursts. Panel (f): rms PF as a function of energy. The pulsation above 10 keV cannot be significantly seen. We estimate 2σ upper limits for the last two energy bins.
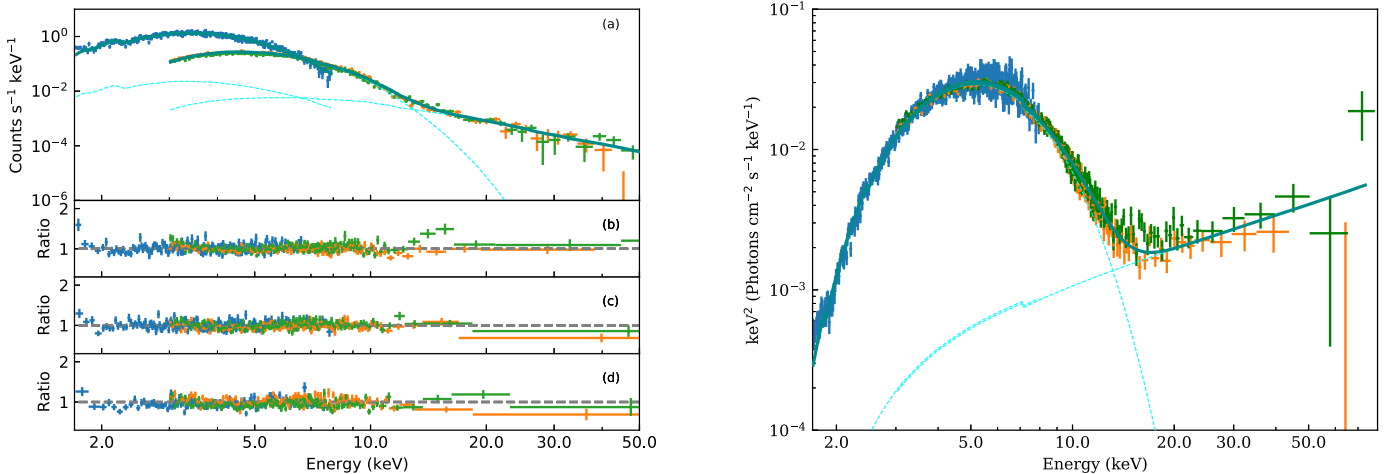
Figure 3. Left: spectral fitting of the joint NICER and NuSTAR data of Swift J1555.2−5402. Panel (a) shows the background-subtracted response-inclusive spectra obtained on June 5 and the best-fit model (dark cyan solid line) with its blackbody and power-law components (cyan dashed lines). Photoelectric absorption is not corrected. Panels (b)–(d) show spectra obtained on June 5, 9, and 21, divided by the best-fit model to the first epoch shown in panel (a). Right: best-fit νF_ν spectra of NICER and NuSTAR FPMA and FPMB for the three epochs combined. In both panels, NICER and NuSTAR FPMA and FPMB data are shown in blue, orange, and green, respectively.

2–8 keV range. Assuming a distance of 10 kpc, the blackbody radius is estimated to be 7.4 ± 1.6 km. The fluences of detected bursts are calculated to be in the range of $(1–13) \times 10^{-10}$ erg cm^{-2} with an assumed blackbody spectrum of $kT = 2.8$ keV using the WebPIMMs Appendix (Appendix Table B2). One of the NICER bursts was simultaneously detected with Swift BAT (Appendix Figure B2).

3.4. DSN Radio Analyses

We dedispersed the data of each epoch with trial Dispersion Measures (DMs) between zero and 5000 pc cm^{-3} and subsequently searched each resulting time series for both periodic and single-pulse emission. We found no statistically significant periods with a signal-to-noise ratio (S/N) above 7.0 after folding individual dedispersed time series modulo period candidates from PRESTO's `accelsearch` package (Ransom et al. 2002). In addition, we folded the dedispersed time series at each DM trial using the timing model from NICER in Table 1 but found no evidence of radio pulsations at the S or X band during any of our observations. For each epoch, we place 7σ upper limits on the magnetar's flux density, assuming a duty cycle of 10% (see Table A4). Based on our longest observation with DSS-43, the 70 m radio telescope in Tidbinbilla, Australia, we obtain 7σ upper limits on the magnetar's flux of <0.043 mJy at the S band and <0.026 mJy at the X band.

We also searched the dedispersed time series at each frequency band for radio bursts using a matched filtering algorithm, where the time series was convolved with boxcar functions with logarithmically spaced widths between $512\,\mu$s and $150\,$ms. Candidates with a detection S/N above 7.0 were saved and classified using the FETCH software package (Agarwal et al. 2020). The dynamic spectra of the candidates were also visually inspected for verification. We detected no radio bursts during the radio observations and placed 7σ upper limits on the fluence of individual bursts during each epoch at both the S and X bands (see Table A4). On 2021 June 5 and 6, we detected two X-ray bursts, with widths of $w = 15.91$ (see Table B2; burst 8) and 0.27 ms (see Table B2; burst 10), during overlapping radio and X-ray observations. However, no prompt radio emission (within $\pm 10\,$s of the X-ray burst time) was detected above a 7σ fluence detection threshold of $1.6\sqrt{w/1\,\mathrm{ms}}$ and $0.61\sqrt{w/1\,\mathrm{ms}}$ Jy ms at the S and X bands, respectively.

3.5. Search for a Counterpart

We searched the Swift archival data for a serendipitous detection of Swift J1555.2−5402 in its quiescent state. Two observations in 2012 (ObsIDs 00042728001 and 00042729001) covered the location of this source as part of the Swift XRT Galactic plane survey program (Reynolds et al. 2013). The total exposure is 1055 s. We find no X-ray source at this position within a $30''$ radius. The 3σ upper limit of the count rate is estimated to be 5.0×10^{-3} counts s^{-1} within this radius. Then, the 3σ upper limits of the 2–10 keV absorbed and absorption-corrected fluxes are calculated to be 5.0×10^{-13} and 9.0×10^{-13} erg s^{-1} cm^{-2}, respectively, on the assumption of an absorbed blackbody spectrum with $N_{\rm H} = 8.72 \times 10^{22}$ cm^{-2} and $kT = 1.1$ keV. Yet the magnetar surface temperature in quiescence is considerably smaller than that during outburst epochs, with an average of about 0.45 keV among the population (Olausen & Kaspi 2014). Hence, we estimate 2–10 keV absorbed and absorption-corrected fluxes of about 2.6×10^{-13} and 1.2×10^{-12} erg s^{-1} cm^{-2}, respectively. This corresponds to an upper limit of the 2–10 keV quiescent X-ray luminosity of 1.5×10^{34} erg s^{-1} (bolometric thermal luminosity of 4.8×10^{34} erg s^{-1}) at 10 kpc.

The characteristic age of Swift J1555.2−5402 is inferred to be 2.01 kyr (see Table 1). If we assume that its true age is comparable to its characteristic age, we expect to find a young supernova remnant (SNR) surrounding the neutron star. Detection of an associated SNR, combined with a possible proper-motion measurement, would be helpful and can be important for constraining the magnetar's true age given that the characteristic age may be unreliable due to underlying assumptions about the neutron star rotation period at the birth and braking index. Our search of archival radio, infrared, and X-ray data (e.g., Green 2019) for an SNR or a pulsar-wind nebula coinciding at the position of Swift J1555.2−5402, $(l, b) = (327.872, -0.335)$ in the galactic coordinates using SkyView[37] fails to yield any convincing candidates.

4. Discussion and Conclusion

4.1. Timing and Spectral Characteristics of the New Magnetar

High-cadence monitoring with NICER over 1 month allows us to measure the spin ephemeris of the new source Swift J1555.2−5402 (Table 1). Refined from the initial reports in GCNs and ATels (Coti Zelati et al. 2021b; Ng et al. 2021), the period and its time derivative are measured to be 3.86104705(12) s and $3.05(7) \times 10^{-11}$ s s^{-1}, respectively. The combination of the two values falls within the distribution of known magnetars on the P–$\dot{P}$ diagram (Figure 4(a)). Assuming the standard rotating magnetic dipole model and a braking index of $n = 3$, these timing parameters correspond to a characteristic age of $\tau = 2.01(5)$ kyr, surface magnetic field strength of $B_{\rm surf} = 3.47(4) \times 10^{14}$ G, and spin-down luminosity of $L_{\rm sd} = 2.09(5) \times 10^{34}$ erg s^{-1}. This source was classified as a magnetar based on the measured strong magnetic field. The derived characteristic age suggests that it is one of the youngest magnetars among the known ones. The suggestion is supported by the observed strong timing noise, which requires a model with high-order polynomials (Section 3.1), similar to that of the young magnetar Swift J1818.0−1607 (Hu et al. 2020). We caution that the derived pulsar parameters during the outburst may deviate from those in the quiescent state (e.g., Younes et al. 2017a; Archibald et al. 2020). Frequency derivatives are known to fluctuate during magnetar outbursts, with variations of a factor of 1–50 (see, e.g., Dib et al. 2012; Dib & Kaspi 2014; Levin et al. 2019). Thus, the accuracy of the inferred parameters $B_{\rm surf} \propto \sqrt{\dot{P}}$, $\tau \propto \dot{P}^{-1}$, and $L_{\rm sd} \propto \dot{P}$ relative to the quiescent values still has uncertainties due to this $\dot{P}$ variation.

We detect a hard X-ray tail above 10 keV with NuSTAR, extending up to at least 40 keV with 3σ significance. The spectral energy distribution shows that the hard X-ray component is distinguished from the blackbody component, which should originate from the stellar surface (Figure 3). The existence of the distinctive hard tail is further supported by the steep drop in the energy-dependent PF above 10 keV (Figure 2(f)). Two-component spectra of this kind are reported from other persistently bright and transient magnetars (Kuiper et al. 2006; Enoto et al. 2010a; Younes et al. 2017b). The lack of pulsations (PF < 10%) in the hard X-rays may suggest that the hard tail originates in magnetospheric emission that does not have much anisotropy and higher emission altitude than emission from the stellar surface. This may imply a low magnetic impact parameter (e.g., Wadiasingh et al. 2018) for the observer across the pulse for resonant Compton scattering. The 15–60 keV flux of Swift J1555.2−5402, $F_{15-60} = 6.21 \pm 0.23 \times 10^{-12}$ erg s^{-1} cm^{-2}, is lower than the absorbed 1–10 keV flux $F_{1-10} = 4.65^{+0.19}_{-0.27} \times 10^{-11}$ erg s^{-1} cm^{-2}. Accordingly, the broadband hardness ratio of the magnetospheric to surface thermal emissions is $\eta = F_{15-60}/F_{1-10} = 0.13$. The hardness ratio η of known magnetars ($\eta = 0.1$–4) is suggested to be correlated with the surface magnetic field. Figure 4(d) plots the η values of known sources and Swift J1555.2−5402. It shows that the η of Swift J1555.2−5402 is not largely off, though apparently smaller than, the proposed correlation (see Equation (3) of Enoto et al. 2017). We note that the measured η has some systematic uncertainty. If the yet-unknown long-term frequency derivative of Swift J1555.2−5402 is lower than the value measured during the current outburst, the magnetic field strength in the quiescent state is weaker than our estimate, which places the η of Swift J1555.2−5402 closer to the known correlation.

4.2. X-Ray Luminosity

Figure 4(b) compares pulsar X-ray luminosity $L_{\rm x}$ with spin-down luminosity $L_{\rm sd}$. Immediately after the outburst, the

---

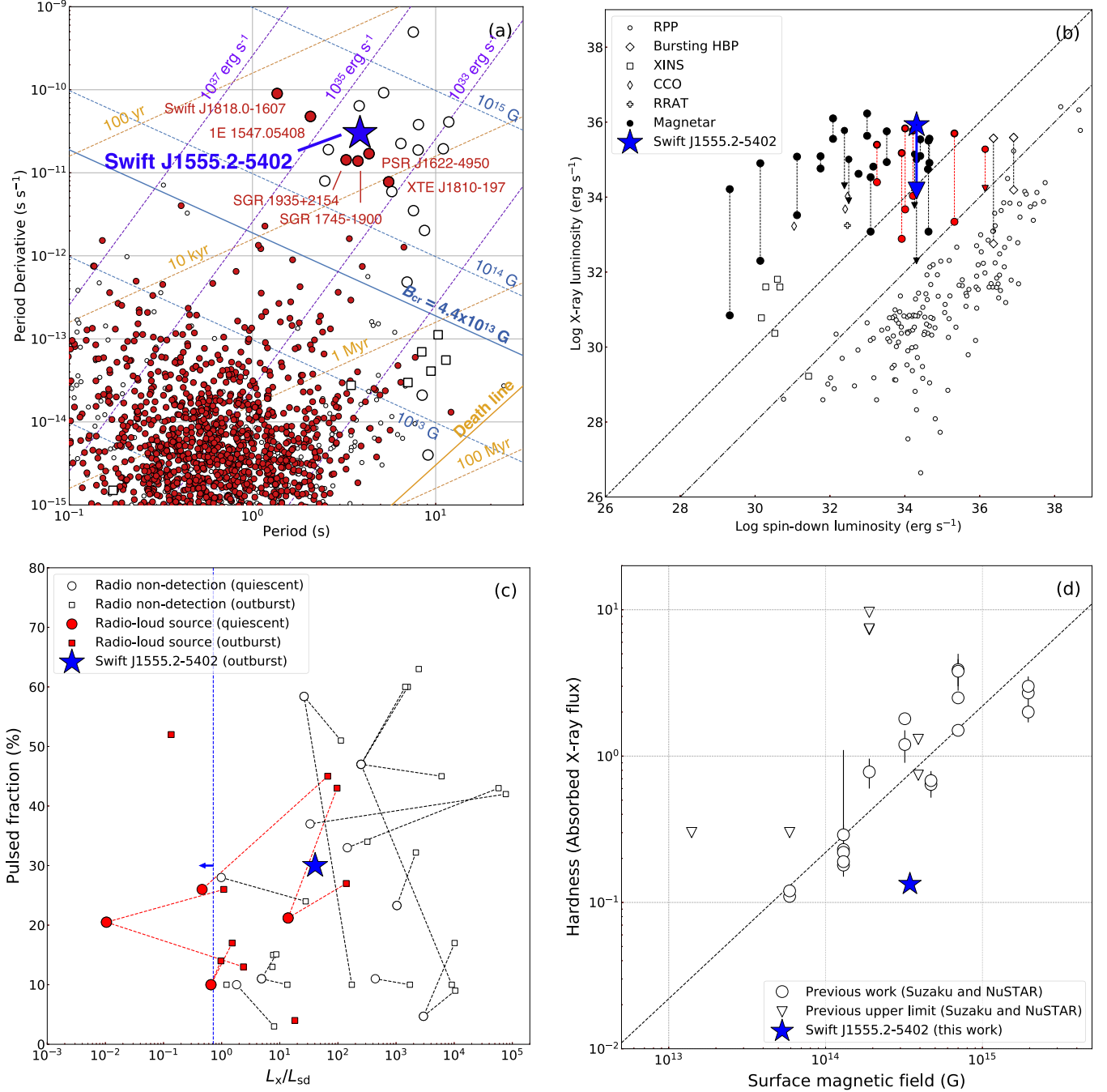[37] https://skyview.gsfc.nasa.gov

Figure 4. (a) Position of the new magnetar Swift J1555.2−5402 (star) on the P–$\dot{P}$ diagram. Large and small circles indicate magnetars (from the McGill catalog; Olausen & Kaspi 2014) and canonical rotation-powered pulsars (from the ATNF catalog; Manchester et al. 2005), respectively. Filled red symbols indicate radio-emitting pulsars. The lines show constant surface magnetic field strengths, characteristic ages, and spin-down luminosities. Squares in panels (a) and (b) are X-ray-dim isolated neutron stars. (b) Observed X-ray luminosity in the soft X-ray band (including the unpulsed component) compared with the spin-down power for various types of pulsars. The peak X-ray luminosity and quiescent values of magnetars are connected via dashed lines. Red symbols indicate radio-loud magnetars. The two diagonal lines indicate where the X-ray luminosity becomes equal to 100% and 1% of the spin-down power. The values and references used in panels (b)–(d) are summarized in Appendix Tables C1 and C2 for magnetars and Enoto et al. (2019) for other pulsars. (c) The PFs as a function of the X-ray luminosity normalized by the spin-down power. Filled red symbols indicate radio-emitting magnetars. Circles and squares represent data in quiescence and during X-ray outbursts, respectively. A dashed line connects observations for the same source. The vertical dashed line with the arrow indicates the region of the quiescent state of Swift J1555.2−5402. (d) Broadband hardness ratio of absorbed X-ray fluxes between 1–10 and 15–60 keV with the best-fit correlation (Enoto et al. 2017).

surface emission (2–10 keV) and total (2–60 keV) luminosity of Swift J1555.2−5402 were $L_x = 8.5 \times 10^{35}d_{10}^2$ and $9.6 \times 10^{35}d_{10}^2$ erg s^{-1}, respectively. At the assumed distance of 10 kpc, these are, respectively, 40 and 46 times larger than its spin-down luminosity $L_{sd} = 2.1 \times 10^{34}$ erg s^{-1}. The observed X-ray luminosity is similar to those of past reported

outbursts of transient magnetars. The upper limit on the quiescent X-ray luminosity of Swift J1555.2−5402 is $L_{quie} \approx 1.5 \times 10^{34}d_{10}^2$, corresponding to $L_{quie}/L_{sd} \lesssim 0.71d_{10}^2$, which is still up to 2−3 orders of magnitude higher than those of the rotation-powered pulsars (see Figure 4(b) and Figure 12 of Enoto et al. 2019). The upper limit on the quiescent

bolometric thermal luminosity $\approx 4.8 \times 10^{34} d_{10}^2$ erg s^{-1} also makes Swift J1555.2−5402 one of the coolest young magnetars (see, e.g., Potekhin et al. 2015) and is compatible with the $L \sim 2 \times 10^{33}$ erg s^{-1} of PSR J1119−6127 (Gonzalez et al. 2005; Ng et al. 2012; Blumer et al. 2021). The upper limit on the quiescent bolometric thermal luminosity $\approx 4.8 \times 10^{34} d_{10}^2$ erg s^{-1} erg s^{-1} is compatible with $L \sim 2 \times 10^{33}$ erg s^{-1} of PSR J1119−6127 (Gonzalez et al. 2005; Ng et al. 2012; Blumer et al. 2021) and could mean that Swift J1555.2−5402 is one of the cooler young magnetars (see, e.g., Potekhin et al. 2015).

4.3. Peculiarities of the Slow Decline Outburst

The persistent X-ray flux of most transient magnetars remains in a bright plateau state for a few weeks immediately after the onset of outbursts and then starts to fade over the next several months (Coti Zelati et al. 2018). Typically, the plateau duration and decaying slope are $\tau_0 = 11$–43 days and $p \sim 0.7$–2 (Enoto et al. 2017), respectively, when the X-ray flux F_x is fitted with an empirical formula $F_x(t) = F_0/(1 + t/\tau_0)^p$, where t and F_0 are the elapsed time and plateau flux, respectively. A peculiarity of Swift J1555.2−5402 is its long-lasting outburst. The absorbed X-ray flux stayed nearly stable at around 4×10^{-11} erg s^{-1} cm^{-2} with only a slow decline over a month. There was no apparent rollover of the flux trend as of July 1. Such long-lasting outbursts are rare for magnetars, with only a few exceptions ever recorded, e.g., the radio-loud magnetar 1E 1547.0−5408.

Another peculiarity of the Swift J1555.2−5402 outburst is the higher temperature ($kT \sim 1.1$ keV) of the blackbody component than the typical value of known magnetars, $kT \sim 0.3$–0.7 keV (Enoto et al. 2017), despite the surface emission radius $R \sim 2d_{10}$ km of Swift J1555.2−5402 being well within the typical range for a neutron star. During the 1 month observation, the slow flux decline originated from the decreasing emission radius rather than the temperature decline. This fact suggests a situation where the hot spot on the neutron star surface responsible for the X-ray emission was shrinking, which is consistent with the twisted magnetosphere model (Kaspi & Beloborodov 2017).

We detected 45 and 5 short bursts with NICER and Swift/BAT, respectively, during the initial 2 weeks since discovery of Swift J1555.2−5402 (Figure 1(j)). The burst-active periods of persistently bright magnetars (e.g., SGR 1806−20) are known to be longer ($\gtrsim 100$ days) than those ($\lesssim 10$ days) of low-burst rate transient ones (e.g., SGR 0501+4516; Göğüş 2014). The burst-active period of Swift J1555.2−5402 is close to the latter case. We conjecture that repeated bursts as observed in Swift J1555.2−5402 would provide impulsive heating of the surface to sustain the long-lasting decay. To investigate the potential relationship between the bursts and persistent emission on the pulse profile, we plot in Figure 2(e) the phase distribution of the observed bursts. An Anderson–Darling (AD) test suggests that the burst phase distribution differs from a uniform distribution with an AD statistic of 0.42 and corresponding p-value of 0.82. Thus, there is neither a statistical difference between the phase distribution of the bursts and uniform distribution nor a statistically significant correlation between the burst occurrence and the pulse profile so far.

4.4. Comparison with Radio-emitting Magnetars

We did not detect any radio emission from this source. It has been long established theoretically that as far as ordinary pulsars are concerned, the occurrence of rotation-powered polar-cap radio emission requires a sufficiently large potential drop $\Delta\Phi$ to generate electron-positron pairs near polar caps (Goldreich & Julian 1969; Sturrock 1971; Ruderman & Sutherland 1975; Arons & Scharlemann 1979); note that the conventional definition of $\Delta\Phi \propto L_{sd}^{1/2}$ implies that radio emission is equivalently related to L_{sd} (Ho 2013). The observed radio luminosity of rotation-powered pulsars indeed follows the relation (e.g., Arzoumanian et al. 2002). In the absence of magnetically induced nonpotential fields, magnetars that satisfy this condition at their polar caps before crossing the death line should, in principle, be capable of producing coherent radio emission. However, as shown in Figures 4(a)–(c) and summarized in Appendix Table C1, pulsed radio emission has only been reported from six radio-loud magnetars and a high-B pulsar that exhibited a magnetar-like outburst. It is an open question under what conditions a magnetar becomes radio-loud. The new magnetar Swift J1555.2−5402 is located in the P–$\dot{P}$ parameter space close to radio-loud magnetars (Figure 4(a)). The DSN upper limits on the radio luminosity ($\nu L_\nu = 1.1 \times 10^{28} d_{10}^2$ erg s^{-1} for the S band and $2.6 \times 10^{28} d_{10}^2$ erg s^{-1} for the X band) would be much lower than those of the known radio-loud magnetars, $\nu L_\nu \sim (0.08$–1$) \times 10^{30}$ and $\sim (0.01$–3$) \times 10^{31}$ erg s^{-1} at the S and X bands, respectively (Camilo et al. 2007a, 2007b, 2008; Levin et al. 2010, 2012; Shannon & Johnston 2013; Pennucci et al. 2015; Huang et al. 2021). Therefore, the lack of radio emission suggests the existence of some other physical factors than simply P and $\dot{P}$ that govern radio emission.

One crucial factor is the geometry among the pulsar rotation axis, magnetic axis, line of sight to the observer, and width of any putative radio beam. For example, an anisotropic radio beam aligned to the magnetic axis must cross the line of sight to be detected, and longer-period rotation-powered pulsars tend to have narrower beams (e.g., Lyne & Manchester 1988; Rankin 1993). The radio nondetection of Swift J1555.2−5402 might suggest that this magnetar may not have a favorable geometry for detection (e.g., Lazarus et al. 2012). Some radio-loud magnetars have observational signatures that suggest aligned rotators (i.e., the angle between the magnetic axis and rotation axis is $\lesssim 30°$; Camilo et al. 2008; Levin et al. 2012; Lower et al. 2020). As shown in Figure 4(c), the PF both in quiescence and during X-ray outbursts of radio-loud magnetars is lower than that of the other magnetars. A low PF could be due to radio-loud magnetars being observed as near-aligned rotators. The same interpretation can be inferred from the systematic Fourier-decomposition study of X-ray profiles of magnetars in quiescence conducted by Hu et al. (2019); radio-loud magnetars have a more sinusoidal pulse profile with a pronounced first Fourier component accompanied by a weaker second component. Another factor for the radio emission is the effects of higher-order (and possibly not curl-free) magnetic field components other than the dipolar field inferred from P–$\dot{P}$, which has already been taken into account. Quantum electrodynamic effects affect the conditions for pair cascades and radio emission when a magnetic field is sufficiently strong, above 10^{13} G. For example, if photon splitting occurs in a region above the critical magnetic field, the way the electron/positron cascade occurs is modified and perhaps quenched, and

radio pulsation may be suppressed (e.g., Baring & Harding 2001). Finally, magnetar magnetospheres are considered to be dynamic, and the radio flux, pulse profile, and polarization swing pattern can change significantly within a few days (e.g., Lower et al. 2021). Future monitoring of this new magnetar, Swift J1555.2−5402, will be important for understanding the conditions for the magnetar radio emission.

Appendix A
List of Observations

Tables A1–A4 summarize the observations of Swift, NICER, NuSTAR, and DSN, respectively, conducted for this campaign as of July 1.

Table A1
A List of Swift ObsIDs of Swift J1555.2−5402

No.	ObsID	Mode	Start Time (UTC)	End Time (UTC)	MJD	Elapsed Days	Exposure (s)	Rate (cps)
1	01053220000	PC	2021-06-03T09:46:24	2021-06-03T11:21:33	59,368.463	0.06	1706	0.69 ± 0.06
2	00014352001	WT	2021-06-04T7:50:02	2021-06-04T9:37:00	59,369.364	1.0	1965	0.52 ± 0.02
3	00014352002	WT	2021-06-05T10:40:43	2021-06-05T15:46:23	59,370.551	2.1	4895	0.51 ± 0.02
4	00014352003	WT	2021-06-07T12:06:00	2021-06-07T13:49:00	59,372.540	4.1	1940	0.53 ± 0.02

Note. MJD: middle of the start and end time of an observation. Elapsed days: elapsed days from the first short burst at MJD 59,368.40678 detected with Swift/BAT. Rate: background-subtracted 2–10 keV count rate of Swift.

Table A2
A List of NICER ObsIDs of Swift J1555.2−5402

No.	ObsID	Start Time (UTC)	End Time (UTC)	MJD	Elapsed Days	Exposure (s)	Rate (cps)
1	4202190101	2021-06-03T11:21:31	2021-06-03T18:52:20	59,368.630	0.2	2367	3.74
2	4560010101	2021-06-04T04:00:20	2021-06-04T14:54:24	59,369.394	1.0	2201	3.91
3	4560010102	2021-06-05T01:25:40	2021-06-05T23:32:00	59,370.520	2.1	7235	3.96
4	4560010103	2021-06-06T02:31:20	2021-06-06T17:31:40	59,371.418	3.0	2068	3.52
5	4560010104	2021-06-07T02:42:51	2021-06-07T23:00:40	59,372.536	4.1	2199	4.07
6	4560010105	2021-06-08T00:24:27	2021-06-08T22:16:20	59,373.472	5.1	2931	3.88
7	4560010201	2021-06-09T04:16:47	2021-06-09T16:53:20	59,374.441	6.0	6070	3.9
8	4560010202	2021-06-10T01:56:20	2021-06-10T14:36:20	59,375.345	6.9	2582	3.94
9	4560010301	2021-06-11T02:43:40	2021-06-11T23:10:00	59,376.539	8.1	1852	4.28
10	4560010601	2021-06-12T08:11:19	2021-06-12T08:27:40	59,377.347	8.9	910	4.18
11	4560010401	2021-06-13T05:52:25	2021-06-13T21:38:20	59,378.573	10.2	988	3.82
12	4560010402	2021-06-14T08:12:26	2021-06-14T20:52:40	59,379.606	11.2	915	3.99
13	4560010501	2021-06-15T15:11:28	2021-06-15T15:28:00	59,380.639	12.2	909	4.53
14	4560010502	2021-06-16T06:41:09	2021-06-16T08:24:28	59,381.314	12.9	1085	4.25
15	4560010602	2021-06-17T02:49:31	2021-06-17T20:08:40	59,382.479	14.1	911	3.3
16	4560010603	2021-06-18T08:15:34	2021-06-18T19:22:40	59,383.576	15.2	998	3.82
17	4560010701	2021-06-19T04:24:22	2021-06-19T06:09:08	59,384.220	15.8	1575	3.7
18	4560010702	2021-06-20T05:10:51	2021-06-20T06:54:08	59,385.252	16.8	1472	3.77
19	4560010801	2021-06-21T05:58:08	2021-06-21T23:17:20	59,386.610	18.2	3756	3.66
20	4560010802	2021-06-22T00:33:27	2021-06-22T10:08:00	59,387.223	18.8	4545	3.64
21	4560010901	2021-06-23T05:59:25	2021-06-23T09:17:56	59,388.319	19.9	1979	3.71
22	4560010902	2021-06-24T03:41:05	2021-06-24T07:01:43	59,389.223	20.8	2307	3.68
23	4560011001	2021-06-26T00:34:00	2021-06-26T00:53:20	59,391.030	22.6	902	3.36
24	4560011002	2021-06-27T06:05:15	2021-06-27T06:19:40	59,392.259	23.9	663	3.49
25	4560011101	2021-06-27T07:38:15	2021-06-27T07:44:28	59,392.320	23.9	176	3.3
26	4560011102	2021-06-28T00:41:00	2021-06-28T02:28:20	59,393.066	24.7	1271	3.21
27	4560011201	2021-06-29T20:04:42	2021-06-29T23:20:24	59,394.905	26.5	367	3.12
28	4560011301	2021-07-01T21:35:48	2021-07-01T23:25:19	59,396.938	28.5	1237	3.31

Note. MJD: middle of the start and end time of an observation. Elapsed days: elapsed days from the first short burst at MJD 59,368.40678 detected with Swift/BAT. Rate: background-subtracted 2–10 keV count rate of NICER.

Table A3
A List of NuSTAR ObsIDs of Swift J1555.2−5402

No.	ObsID	Start Time (UTC)	End Time (UTC)	MJD Start	Exposure (ks)	Rate A (cps)	Rate B (cps)
1	90701319002	2021-06-05T10:20:48	2021-06-06T06:33:07	59,370.43111111	38.4	1.12	1.03
2	80702313002	2021-06-09T05:39:00	2021-06-09T18:00:00	59,374.23541667	25.0	1.09	1.025
3	80702313004	2021-06-21T14:05:11	2021-06-22T04:15:00	59,386.58693287	28.9	0.99	0.94

Note. Rates A and B are the 3–79 keV count rate of NuSTAR FPMA and FPMB, respectively.

Table A4
A List of Radio Observations of Swift J1555.2−5402 with the DSN

No.	Instrument	Observation Start Time (UTC)	Observation Start Time (MJD)	Duration (hr)	Observing Frequency Band[a]	Mean Flux Density[b] ($S_{\mathrm{mean}}^{S\text{-band}}$ /$S_{\mathrm{mean}}^{X\text{-band}}$) (mJy/mJy)	Radio Burst Fluence[c] ($\mathcal{F}^{S\text{-band}}$ /$\mathcal{F}^{X\text{-band}}$) (Jy ms/Jy ms)
1	DSN (DSS-36)	2021 Jun 4 06:59:02	59,369.29099	1.3	S band/X band	<0.27/<0.10	<1.7/<0.7
2	DSN (DSS-36)	2021 Jun 5 11:46:10	59,370.49039	2.4	S band/X band	<0.18/<0.07	<1.6/<0.61
3	DSN (DSS-43)	2021 Jun 6 04:49:06	59,371.20076	2.2	S band/X band	<0.042/<0.025	<0.35/<0.21
4	DSN (DSS-34)	2021 Jun 10 11:31:12	59,375.48000	2.4	S band/X band	<0.20/<0.11	<1.7/<0.9
5	DSN (DSS-43)	2021 Jun 12 04:08:52	59,377.17282	2.5	S band/X band	<0.043/<0.026	<0.39/<0.24

Notes. The first two observations (2021 June 4 and 5) and the fourth observation (2021 June 10) were carried out using DSS-36 and DSS-34, two 34 m diameter radio telescopes in Canberra, Australia, whereas the remaining observations (2021 June 6, and 12) were carried out using DSS-43, the 70 m diameter dish in Canberra.
[a] The center frequencies at the S/X bands are 2.2/8.4 GHz, respectively.
[b] The 7σ upper limits on the mean flux density in each radio frequency band, assuming a 10% duty cycle. The uncertainties on the mean flux density upper limits are estimated at 15%, primarily due to the uncertainty in the system temperature.
[c] The 7σ upper limits on the radio burst fluence in each radio frequency band, assuming a burst width of 1 ms. The uncertainties on the fluence detection thresholds are estimated at 15%, primarily due to the uncertainty in the system temperature.

Appendix B
Burst Analyses

Tables B1 and B2 summarize the detected magnetar short bursts by Swift/BAT and NICER, respectively. For the burst search, we recalibrate the event files using `nicerl2` with criteria of `elv=30 br_earth=30 underonly_range=0–300 overonly_range=0-2 overonly_expr=``2.0''` to maximize the time coverage. The corresponding integrated fluence distribution detected with NICER is shown in Figure B1. It shows a power law–like distribution with a low-fluence
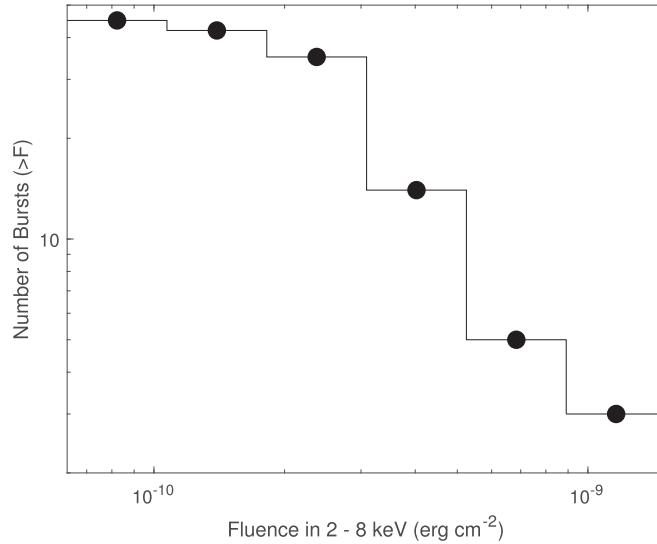

Figure B1. Integrated fluence distribution in 2–8 keV of the detected short bursts from Swift J1555.2−5402 obtained with NICER.
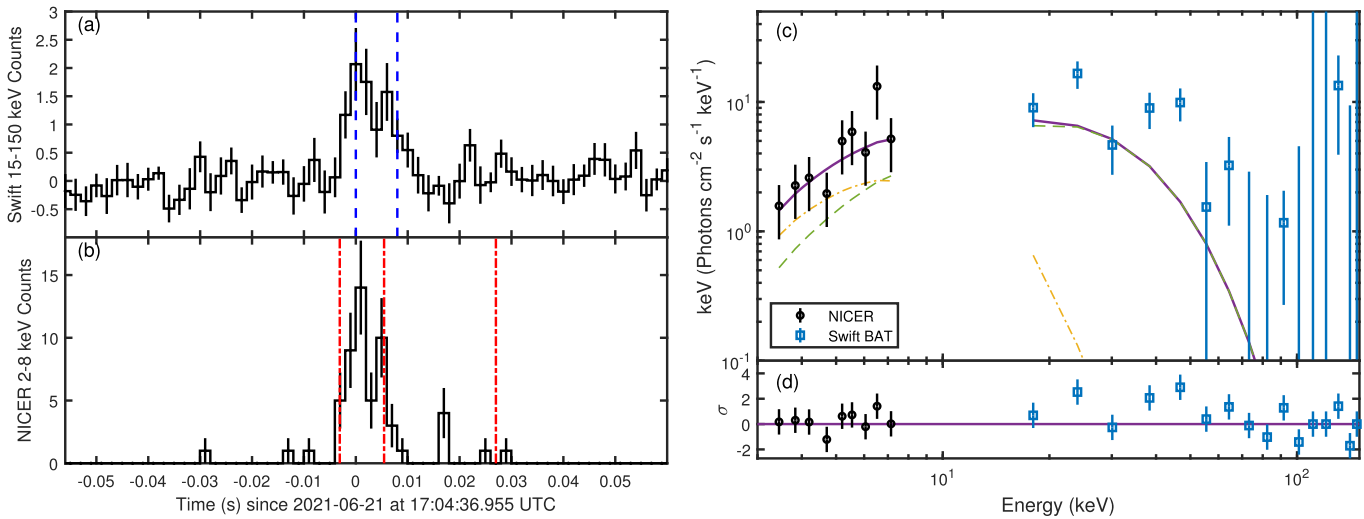
Figure B2. Light curves of a burst detected simultaneously with (a) Swift BAT in 15–150 keV, burst number 5 in Table B1, and (b) NICER in 2–8 keV, numbers 32 and 33 in Table B2. The bin size of the light curves is 2 ms. Blue dashed lines denote the start and end of T_{90} of the Swift light curve, where the red dashed–dotted lines are the boundaries of Bayesian blocks detected with NICER events. The broadband X-ray spectrum of this burst is shown in panel (c), with the best-fit model (purple solid line) consisting of two blackbodies (orange dashed–dotted line and green dashed line). The residuals are shown in panel (d).

Table B1
A List of Short Bursts from Swift J1555.2−5402 Detected with Swift/BAT

No.	Trigger ID	Time (UTC)	Duration T_{90} (ms)	S/N	kT (keV)	Fluence	χ^2
1	1053220	2021-06-03T09:45:46.589	12 ± 2.8	9.9	6.66 ± 0.98	9.09 ± 2.32	33.98
2	1053653	2021-06-05T23:52:04.582	14 ± 4.5	7.3	8.53 ± 1.40	7.47 ± 2.62	28.54
3	1053961	2021-06-07T12:33:40.020	4 ± 2.2	5.0	N/A[a]	N/A[a]	N/A[a]
4	1056025	2021-06-16T14:44:30.489	7 ± 2.8	6.9	6.58 ± 2.22	<3.08	31.20
5	1057131	2021-06-21T17:04:36.839	12 ± 4.5	6.9	6.47 ± 2.03	<3.82	55.54

Notes. Reported errors are 90% confidence for each parameter. Time: burst detection time (UTC) determined as the start time of T_{90}. S/N: Signal-to-noise ratio of the BAT image in 15–350 keV. kT: blackbody temperature (keV) when fitted by the single blackbody model. Fluence: burst fluence in the 15–150 keV band (10^{-9} erg cm^{-2}). χ^2: fitting χ^2 values for 57 dof.
[a] Burst 3 is too weak to constrain the spectral-fit parameters.

Table B2
A List of Short Bursts from Swift J1555.2−5402 Detected with NICER

No.	ObsID	Time (UTC)	Duration (ms)	Significance σ	Phase	Fluence
1	4202190101	2021-06-03T13:51:09.341	14.94	8.80	0.085	2.6 ± 0.8
2	4202190101	2021-06-03T13:51:27.181	59.18	6.38	0.711	2.4 ± 0.8
3	4202190101	2021-06-03T13:54:40.275	19.79	15.47	0.717	6.3 ± 1.3
4	4202190101	2021-06-03T14:01:50.242	12.95	6.75	0.076	1.9 ± 0.7
5	4202190101	2021-06-03T18:49:06.251	35.90	6.35	0.166	1.9 ± 0.7
6	4560010101	2021-06-04T14:37:30.785	18.43	6.91	0.874	1.9 ± 0.7
7	4560010101	2021-06-04T14:43:50.878	15.12	11.32	0.316	4.0 ± 1.0
8	4560010102	2021-06-05T05:57:03.457	49.87	6.19	0.449	2.1 ± 0.7
9[a]	4560010102	2021-06-05T13:55:42.156	15.91	5.67	0.504	1.3 ± 0.6
10	4560010102	2021-06-05T15:42:02.189	14.03	6.67	0.910	1.9 ± 0.7
11	4560010102	2021-06-05T15:43:00.342	16.03	7.43	0.971	1.9 ± 0.7
12	4560010102	2021-06-05T17:12:27.003	1.35	5.50	0.919	0.8 ± 0.5
13	4560010102	2021-06-05T21:55:06.519	98.82	6.41	0.391	2.6 ± 0.8
14	4560010102	2021-06-05T23:31:46.102	34.26	6.50	0.454	2.4 ± 0.8
15[b]	4560010103	2021-06-06T05:36:42.18	0.27	10.62	0.523	2.1 ± 0.7
16	4560010105	2021-06-08T11:19:42.895	9.55	7.63	0.285	1.9 ± 0.7
17	4560010105	2021-06-08T11:23:17.712	3.20	5.95	0.922	1.1 ± 0.5
18	4560010201	2021-06-09T05:51:19.191	19.64	10.85	0.299	4.2 ± 1.1
19	4560010201	2021-06-09T07:24:11.030	7.34	6.13	0.375	1.3 ± 0.6
20	4560010201	2021-06-09T10:34:21.954	7.21	6.50	0.747	1.3 ± 0.6
21	4560010201	2021-06-09T13:41:17.195	25.52	8.77	0.438	3.2 ± 0.9
22	4560010201	2021-06-09T13:42:48.797	19.87	6.18	0.162	1.6 ± 0.6
23	4560010202	2021-06-10T02:00:03.424	14.08	6.89	0.687	1.9 ± 0.7
24	4560010202	2021-06-10T05:05:18.924	21.26	6.24	0.540	1.9 ± 0.7
25	4560010301	2021-06-11T10:39:52.520	6.94	6.11	0.570	1.3 ± 0.6
26	4560010602	2021-06-17T02:51:59.547	6.71	16.58	0.542	6.6 ± 1.3
27	4560010602	2021-06-17T02:53:19.142	54.05	19.37	0.162	13.2 ± 1.9
28	4560010602	2021-06-17T02:59:19.487	72.30	7.00	0.493	2.6 ± 0.8
29	4560010701	2021-06-19T04:33:05.105	7.04	7.19	0.028	1.6 ± 0.6
30	4560010701	2021-06-19T04:40:15.346	7.71	7.19	0.457	1.9 ± 0.7
31	4560010701	2021-06-19T06:07:18.896	23.03	9.82	0.305	3.4 ± 1.0
32[c]	4560010801	2021-06-21T17:04:36.952	8.54	20.58	0.664	10.8 ± 1.7
32-1[d]	4560010801	2021-06-21T17:04:36.960	21.55	6.25	0.668	2.6 ± 0.8
33	4560010801	2021-06-21T23:05:26.979	17.84	6.39	0.767	1.6 ± 0.6
34	4560010801	2021-06-21T23:06:53.759	35.45	8.78	0.244	3.2 ± 0.9
35	4560010802	2021-06-22T00:35:18.974	12.50	8.94	0.228	2.4 ± 0.8
36	4560010802	2021-06-22T00:45:29.330	15.47	8.55	0.307	2.6 ± 0.8
37	4560010802	2021-06-22T02:20:44.171	32.71	8.16	0.385	2.9 ± 0.9
38	4560010802	2021-06-22T03:55:16.474	30.36	10.37	0.445	4.0 ± 1.0
39	4560010802	2021-06-22T08:26:59.567	6.15	12.71	0.746	4.0 ± 1.0
40	4560010802	2021-06-22T08:29:34.911	49.79	19.15	0.984	10.6 ± 1.7
41	4560010802	2021-06-22T10:00:07.220	15.05	8.79	0.882	2.6 ± 0.8
42	4560010902	2021-06-24T06:50:27.424	5.97	5.68	0.654	1.1 ± 0.5
43	4560011001	2021-06-26T00:52:34.199	12.48	9.24	0.167	2.6 ± 0.8
44	4560011301	2021-07-01T21:40:50.682	211.22	7.86	0.284	4.0 pm 1.0
45	4560011301	2021-07-01T23:21:28.122	5.28	12.89	0.860	4.2 ± 1.1

Notes. Time: burst detection time (UTC) determined as the start time of the Bayesian block. Duration: duration between two consecutive Bayesian blocks. Significance: detection significance of the burst from Poisson-distributed noise. Fluence: burst fluence in the 2–8 keV band (10^{-10} erg cm^{-2}) estimated from the number of photons and assuming a blackbody spectrum with $kT = 2.8$ keV. The uncertainty is simply calculated from the Poisson noise, i.e., the square root of the number of photons.
[a] This burst was simultaneously observed with the second observation of DSN (Table A4).
[b] This burst was simultaneously observed with the third observation of DSN (Table A4).
[c] This burst was simultaneously observed with Swift BAT (burst 5 in Table B1).
[d] This candidate is the tail of burst 27.

turnover, which may be caused by the detection limit of NICER. We fit the tail and found a power-law index of -1.5 ± 0.2. The uncertainty is estimated from 10^4 times of Monte Carlo simulations. In each run, we simulate 45 bursts, and the number of photons of each burst is simulated from Poisson-distributed noise with a mean value the same as the observed one. Then we rebin the distribution and obtain the power-law index with data points with a fluence higher than 2×10^{-10} erg cm^{-2}.

A burst (burst number 5 in Table B1 and 32 in Table B2) is simultaneously detected with Swift BAT and NICER. The light

curves of this simultaneous event are shown in Figure B2(a) and (b). We extracted the broadband X-ray spectrum and fit it with an absorbed power law and set $N_H = 8.72 \times 10^{22} \, \mathrm{cm}^{-2}$ (see Figures B2(c) and (d)). The spectrum can be fitted by two blackbodies, although the normalization cannot be well constrained. The soft one has a temperature of $kT = 2.5^{+3.3}_{-0.7}$ keV, which is set to be 0.37 times the temperature of the hard component (Nakagawa et al. 2009). On the other hand, the

spectrum can also be well fitted by an absorbed blackbody with $kT = 5.3 \pm 0.8$ keV and a radius of 7.0 ± 1.6 km at 10 kpc.

Appendix C
Comparison with Previous Magnetar Outbursts

Tables C1 and C2 summarize the properties of previous magnetar outbursts.

Table C1
A List of X-Ray Outbursts of Radio-loud Transient Magnetars

Source	State	L_x (erg s^{-1})	L_{sd} (erg s^{-1})	Distance (kpc)	PF	Energy (keV)	References
1E 1547.0−5408	Quiescent	2.2×10^{33}	2.11×10^{35}	4.5	0.205	0.5–2	1, 2
	Outburst (2008)	2.3×10^{35}			0.26	0.5–10	1, 3
	Outburst (2009)	5.0×10^{35}			0.13	0.5–3	1, 4
XTE J1810−197	Quiescent	2.5×10^{34}	1.80×10^{33}	3.5	0.212	0.5–2	1, 2
	Outburst (2003)	1.7×10^{35}			0.43	1–1.5	1, 5
	Outburst (2018)	2.5×10^{35}			0.27	0.5–2	6, 7
PSR J1622−4950	Quiescent	$< 7.7 \times 10^{32}$	8.27×10^{33}	9			8
	Outburst (2017)	1.5×10^{35}			0.04	0.3–6	8
SGR 1745−1900	Quiescent	4.7×10^{33}	1.02×10^{34}	8.3	0.26	0.5–7	2, 9
	Outburst (2013)	6.8×10^{35}			0.45	0.3–3.5	1, 10
Swift J1818.0−1607	Quiescent	$< 1.7 \times 10^{34}$	1.40×10^{36}	6.5			11
	Outburst (2020)	1.9×10^{35}			0.52	1–3	11, 12
SGR 1935+2154	Quiescent	1.1×10^{34}	1.65×10^{34}	9	0.1	0.5–2	2, 13
	Outburst (2014)	2.5×10^{34}			0.17	0.5–1.5	1, 14
	Outburst (2020)	1.6×10^{34}			0.14	0.7–3	13, 15
PSR J1119−6127	Quiescent	5.7×10^{32}	2.33×10^{36}	8.4	0.74	0.5–2	1, 16
	Outburst (2016)	3.7×10^{35}			0.67	0.7–3	1, 17

Note. L_x: observed X-ray luminosity (0.3–10 keV) assuming the distance in the right column. L_{sd}: spin-down luminosity. PF: X-ray PF defined in the energy band in the right column.

References. 1. Coti Zelati et al. (2018); 2. Hu et al. (2019); 3. Israel et al. (2010); 4. Bernardini et al. (2011); 5. Gotthelf et al. (2004); 6. Pearlman et al. (2020); 7. Borghese et al. (2021); 8. Camilo et al. (2018); 9. Rea et al. (2020); 10. Coti Zelati et al. (2015); 11. Hu et al. (2020); 12. Esposito et al. (2020); 13. Borghese et al. (2020); 14. Israel et al. (2016); 15. Göğüş et al. (2020); 16. Gonzalez et al. (2005); 17. Archibald et al. (2018).

Table C2
A List of X-Ray Outbursts of Radio-quiet Transient Magnetars

Source	State	$L_{\rm x}$ (erg s^{-1})	$L_{\rm sd}$ (erg s^{-1})	Distance (kpc)	PF	Energy (keV)	References
Swift J1555.2−5402	Outburst (2021)	9.7×10^{35}	1.82×10^{34}	10	0.15	1–2	This work
SGR 0418+5729	Quiescent	7.0×10^{30}	2.11×10^{29}	2	0.37	0.5–2	1, 2
	Outburst (2009)	1.6×10^{34}			0.42	1.5–2.5	1, 3
SGR 0501+4516	Quiescent	1.2×10^{33}	1.22×10^{33}	1.5	0.28	0.5–2	1, 2
	Outburst (2008)	3.4×10^{34}			0.24	0.3–2	1, 4
1E 1048.1−5937	Quiescent	8.6×10^{34}	3.29×10^{33}	9	0.584	0.5–2	1, 2
	Outburst (2011)	5.7×10^{35}			0.10	1–10	1, 5
	Outburst (2016)	3.7×10^{35}			0.51	3–7	1, 6
CXOU J164710.2−455216	Quiescent	3.3×10^{33}	1.32×10^{31}	4	0.47	0.5–2	1, 2
	Outburst (2006)	1.2×10^{35}			0.10	0.5–4	1, 7
	Outburst (2011)	2.1×10^{34}			0.60	0.5–4	1, 7
	Outburst (2017)	1.9×10^{34}			0.60	0.3–2.5	8
	Outburst (2018)	8.0×10^{34}			0.45	0.3–2.5	8
SGR 1806−20	Quiescent	8.2×10^{34}	4.54×10^{34}	8.7	0.1	0.5–4	1, 2
	Outburst (2004)	3.6×10^{35}			0.03	2–10	1, 9
Swift J1822.3−1606	Quiescent	2.0×10^{32}	1.38×10^{30}	1.6	0.33	0.5–2	1, 2
	Outburst (2011)	8.0×10^{34}			0.43	2–8	1, 10
1E 2259+586	Quiescent	5.8×10^{34}	5.61×10^{31}	3.2	0.233	0.5–2	1, 2
	Outburst (2002)	1.2×10^{35}			0.322	0.1–2	1, 11
SGR 1627−41	Quiescent	1.2×10^{33}	4.29×10^{34}	11			1
	Outburst (1998)	5.2×10^{34}			0.10	0.1–10	1, 12
	Outburst (2008)	3.2×10^{35}			0.13	2–10	1, 13
SGR 1833−0832	Quiescent	$< 8.0 \times 10^{33}$	3.18×10^{32}	10			1
	Outburst (2010)	1.0×10^{35}			0.34	0.2–4	1, 14
Swift J1834.9−0846	Quiescent	$< 2.0 \times 10^{32}$	2.05×10^{34}	4.2			1
	Outburst (2011)	1.0×10^{35}			0.85	2–10	1, 15
SGR 1830−0645	Quiescent	$< 2.0 \times 10^{34}$	2.44×10^{32}	10			16
	Outburst (2020)	6.0×10^{35}			0.63	0.3–2	16
SGR 1900+14	Quiescent	1.3×10^{35}	2.58×10^{34}	12.5	0.11	0.5–2	1, 2
	Outburst (2001)	3.5×10^{35}			0.10	0.8–6.5	1, 17
	Outburst (2006)	2.4×10^{35}			0.151	0.8–4	1, 18
1E 1841−045	Quiescent	4.3×10^{35}	9.84×10^{32}	8.5	0.11	0.5–2	1, 2
	Outburst (2011)	1.7×10^{36}			0.10	0.5–2	1, 19
4U 0142+61	Quiescent	3.6×10^{35}	1.21×10^{32}	3.6	0.047	0.5–2	1, 2
	Outburst (2011)	1.2×10^{36}			0.17	0.7–10	1, 20
	Outburst (2015)	1.3×10^{36}			0.09	0.7–10	1, 20

Note. Definitions of the columns are the same as in Table C1.

References. 1. Coti Zelati et al. (2018); 2. Hu et al. (2019); 3. Esposito et al. (2010); 4. Göğüş et al. (2010b); 5. Archibald et al. (2015); 6. Archibald et al. (2020); 7. Rodríguez Castillo et al. (2014); 8. Borghese et al. (2019); 9. Woods et al. (2007); 10. Livingstone et al. (2011); 11. Zhu et al. (2008); 12. Woods et al. (1999); 13. Esposito et al. (2009); 14. Göğüş et al. (2010a); 15. Kargaltsev et al. (2012); 16. Coti Zelati et al. (2021a); 17. Göğüş et al. (2011); 18. Mereghetti et al. (2006); 19. An et al. (2013); 20. Archibald et al. (2017).

ORCID iDs

Teruaki Enoto https://orcid.org/0000-0003-1244-3100
Mason Ng https://orcid.org/0000-0002-0940-6563
Chin-Ping Hu https://orcid.org/0000-0001-8551-2002
Tolga Güver https://orcid.org/0000-0002-3531-9842
Gaurava K. Jaisawal https://orcid.org/0000-0002-6789-2723
Brendan O'Connor https://orcid.org/0000-0002-9700-0036
Ersin Göğüş https://orcid.org/0000-0002-5274-6790
Shota Kisaka https://orcid.org/0000-0002-2498-1937
Zorawar Wadiasingh https://orcid.org/0000-0002-9249-0515
Walid A. Majid https://orcid.org/0000-0002-4694-4221
Aaron B. Pearlman https://orcid.org/0000-0002-8912-0732
Karishma Bansal https://orcid.org/0000-0002-7418-7862
Harsha Blumer https://orcid.org/0000-0003-4046-884X
Deepto Chakrabarty https://orcid.org/0000-0001-8804-8946

Keith Gendreau https://orcid.org/0000-0001-7115-2819
Wynn C. G. Ho https://orcid.org/0000-0002-6089-6836
Chryssa Kouveliotou https://orcid.org/0000-0003-1443-593X
Paul S. Ray https://orcid.org/0000-0002-5297-5278
Tod E. Strohmayer https://orcid.org/0000-0001-7681-5845
George Younes https://orcid.org/0000-0002-7991-028X
David M. Palmer https://orcid.org/0000-0001-7128-0802
Takanori Sakamoto https://orcid.org/0000-0001-6276-6616
Takuya Akahori https://orcid.org/0000-0001-9399-5331
Sujin Eie https://orcid.org/0000-0003-0340-0651

References

Agarwal, D., Aggarwal, K., Burke-Spolaor, S., Lorimer, D. R., & Garver-Daniels, N. 2020, MNRAS, 497, 1661
An, H., Hascoët, R., Kaspi, V. M., et al. 2013, ApJ, 779, 163
Archibald, R. F., Kaspi, V. M., Ng, C. Y., et al. 2015, ApJ, 800, 33
Archibald, R. F., Kaspi, V. M., Scholz, P., et al. 2017, ApJ, 834, 163

Archibald, R. F., Kaspi, V. M., Tendulkar, S. P., & Scholz, P. 2018, ApJ, 869, 180
Archibald, R. F., Scholz, P., Kaspi, V. M., Tendulkar, S. P., & Beardmore, A. P. 2020, ApJ, 889, 160
Arnaud, K. A. 1996, in ASP Conf. Ser. 101, Astronomical Data Analysis Software and Systems V, ed. G. H. Jacoby & J. Barnes (San Francisco, CA: ASP), 17
Arons, J., & Scharlemann, E. T. 1979, ApJ, 231, 854
Arzoumanian, Z., Chernoff, D. F., & Cordes, J. M. 2002, ApJ, 568, 289
Astropy Collaboration, Robitaille, T. P., Tollerud, E. J., et al. 2013, A&A, 558, A33
Bansal, K., Pearlman, A. B., Majid, W. A., et al. 2021, ATel, 14678, 1
Baring, M. G., & Harding, A. K. 2001, ApJ, 547, 929
Barthelmy, S. D., Barbier, L. M., Cummings, J. R., et al. 2005, SSRv, 120, 143
Beloborodov, A. M., & Li, X. 2016, ApJ, 833, 261
Bernardini, F., Israel, G. L., Stella, L., et al. 2011, A&A, 529, A19
Bildsten, L., Chakrabarty, D., Chiu, J., et al. 1997, ApJS, 113, 367
Blumer, H., Safi-Harb, S., Borghese, A., et al. 2021, arXiv:2106.12018
Bochenek, C. D., Ravi, V., Belov, K. V., et al. 2020, Natur, 587, 59
Borghese, A., Coti Zelati, F., Rea, N., et al. 2020, ApJL, 902, L2
Borghese, A., Rea, N., Turolla, R., et al. 2019, MNRAS, 484, 2931
Borghese, A., Rea, N., Turolla, R., et al. 2021, MNRAS, 504, 5244
Buccheri, R., Bennett, K., Bignami, G. F., et al. 1983, A&A, 128, 245
Burgay, M., Pilia, M., Possenti, A., et al. 2021, ATel, 14680, 1
Burrows, D. N., Hill, J. E., Nousek, J. A., et al. 2005, SSRv, 120, 165
Camilo, F., Ransom, S. M., Halpern, J. P., & Reynolds, J. 2007a, ApJL, 666, L93
Camilo, F., Ransom, S. M., Peñalver, J., et al. 2007b, ApJ, 669, 561
Camilo, F., Reynolds, J., Johnston, S., Halpern, J. P., & Ransom, S. M. 2008, ApJ, 679, 681
Camilo, F., Scholz, P., Serylak, M., et al. 2018, ApJ, 856, 180
CHIME/FRB Collaboration, Andersen, B. C., Bandura, K. M., et al. 2020, Natur, 587, 54
Coti Zelati, F., Borghese, A., Israel, G. L., et al. 2021a, ApJL, 907, L34
Coti Zelati, F., Borghese, A., Rea, N., et al. 2021b, ATel, 14674, 1
Coti Zelati, F., Rea, N., Papitto, A., et al. 2015, MNRAS, 449, 2685
Coti Zelati, F., Rea, N., Pons, J. A., Campana, S., & Esposito, P. 2018, MNRAS, 474, 961
Dib, R., & Kaspi, V. M. 2014, ApJ, 784, 37
Dib, R., Kaspi, V. M., Scholz, P., & Gavriil, F. P. 2012, ApJ, 748, 3
Enoto, T., Kisaka, S., & Shibata, S. 2019, RPPh, 82, 106901
Enoto, T., Nakazawa, K., Makishima, K., et al. 2010a, ApJL, 722, L162
Enoto, T., Nakazawa, K., Makishima, K., et al. 2010b, PASJ, 62, 475
Enoto, T., Shibata, S., Kitaguchi, T., et al. 2017, ApJS, 231, 8
Esposito, P., Burgay, M., Possenti, A., et al. 2009, MNRAS, 399, L44
Esposito, P., Israel, G. L., Turolla, R., et al. 2010, MNRAS, 405, 1787
Esposito, P., Rea, N., Borghese, A., et al. 2020, ApJL, 896, L30
Evans, P. A. 2021, ATel, 14675, 1
Gehrels, N., Chincarini, G., Giommi, P., et al. 2004, ApJ, 611, 1005
Gelfand, J. D., & Gaensler, B. M. 2007, ApJ, 667, 1111
Gendreau, K. C., Arzoumanian, Z., Adkins, P. W., et al. 2016, Proc. SPIE, 9905, 99051H
Goldreich, P., & Julian, W. H. 1969, ApJ, 157, 869
Gonzalez, M. E., Kaspi, V. M., Camilo, F., Gaensler, B. M., & Pivovaroff, M. J. 2005, ApJ, 630, 489
Gotthelf, E. V., Halpern, J. P., Buxton, M., & Bailyn, C. 2004, ApJ, 605, 368
Göğüş, E., Baring, M. G., Kouveliotou, C., et al. 2020, ApJL, 905, L31
Göğüş, E. 2014, AN, 335, 296
Göğüş, E., Cusumano, G., Levan, A. J., et al. 2010a, ApJ, 718, 331
Göğüş, E., Güver, T., Özel, F., Eichler, D., & Kouveliotou, C. 2011, ApJ, 728, 160
Göğüş, E., Woods, P. M., Kouveliotou, C., et al. 2010b, ApJ, 722, 899
Green, D. A. 2019, JApA, 40, 36
Harrison, F. A., Craig, W. W., Christensen, F. E., et al. 2013, ApJ, 770, 103
Ho, W. C. G. 2013, MNRAS, 429, 113
Hu, C.-P., Begiçarslan, B., Güver, T., et al. 2020, ApJ, 902, 1
Hu, C.-P., Ng, C. Y., & Ho, W. C. G. 2019, MNRAS, 485, 4274
Huang, Z.-P., Yan, Z., Shen, Z.-Q., et al. 2021, MNRAS, 505, 1311
Israel, G. L., Esposito, P., Rea, N., et al. 2010, MNRAS, 408, 1387
Israel, G. L., Esposito, P., Rea, N., et al. 2016, MNRAS, 457, 3448
Israel, G. L., Zelati, F. C., Borghese, A., et al. 2021, ATel, 14685, 1
Kargaltsev, O., Kouveliotou, C., Pavlov, G. G., et al. 2012, ApJ, 748, 26
Kaspi, V. M., & Beloborodov, A. M. 2017, ARA&A, 55, 261
Kouveliotou, C., Dieters, S., Strohmayer, T., et al. 1998, Natur, 393, 235
Kuiper, L., Hermsen, W., den Hartog, P. R., & Collmar, W. 2006, ApJ, 645, 556
Lazarus, P., Kaspi, V. M., Champion, D. J., Hessels, J. W. T., & Dib, R. 2012, ApJ, 744, 97
Levin, L., Bailes, M., Bates, S., et al. 2010, ApJL, 721, L33
Levin, L., Bailes, M., Bates, S. D., et al. 2012, MNRAS, 422, 2489
Levin, L., Lyne, A. G., Desvignes, G., et al. 2019, MNRAS, 488, 5251
Li, C. K., Lin, L., Xiong, S. L., et al. 2021, NatAs, 5, 378
Lien, A., Sakamoto, T., Barthelmy, S. D., et al. 2016, ApJ, 829, 7
Livingstone, M. A., Scholz, P., Kaspi, V. M., Ng, C. Y., & Gavriil, F. P. 2011, ApJL, 743, L38
Lower, M. E., Johnston, S., Shannon, R. M., Bailes, M., & Camilo, F. 2021, MNRAS, 502, 127
Lower, M. E., Shannon, R. M., Johnston, S., & Bailes, M. 2020, ApJL, 896, L37
Luo, J., Ransom, S., Demorest, P., et al. 2021, ApJ, 911, 45
Lyne, A. G., & Manchester, R. N. 1988, MNRAS, 234, 477
Majid, W. A., Pearlman, A. B., Dobreva, T., et al. 2017, ApJL, 834, L2
Manchester, R. N., Hobbs, G. B., Teoh, A., & Hobbs, M. 2005, AJ, 129, 1993
Mereghetti, S. 2008, A&ARv, 15, 225
Mereghetti, S., Esposito, P., Tiengo, A., et al. 2006, ApJ, 653, 1423
Mereghetti, S., Savchenko, V., Ferrigno, C., et al. 2020, ApJL, 898, L29
Nakagawa, Y. E., Yoshida, A., Yamaoka, K., & Shibazaki, N. 2009, PASJ, 61, 109
Nasa High Energy Astrophysics Science Archive Research Center (Heasarc) 2014, HEAsoft: Unified Release of FTOOLS and XANADU, Astrophysics Source Code Library, ascl:1408.004
Ng, C. Y., Kaspi, V. M., Ho, W. C. G., et al. 2012, ApJ, 761, 65
Ng, M., Hu, C. P., Enoto, T., et al. 2021, ATel, 14684, 1
Olausen, S. A., & Kaspi, V. M. 2014, ApJS, 212, 6
Palmer, D. 2021, ATel, 14690, 1
Palmer, D. M., Evans, P. A., Kuin, N. P. M., Page, K. L. & Swift Team 2021, GCN Circ., 30120, 1, https://gcn.gsfc.nasa.gov/other/SGRJ1555.2-5402.gcn3
Pearlman, A. B., Majid, W. A., & Prince, T. A. 2019, AdAst, 2019, 6325183
Pearlman, A. B., Majid, W. A., Prince, T. A., et al. 2020, arXiv:2005.08410
Pearlman, A. B., Majid, W. A., Prince, T. A., Kocz, J., & Horiuchi, S. 2018, ApJ, 866, 160
Pennucci, T. T., Possenti, A., Esposito, P., et al. 2015, ApJ, 808, 81
Perna, R., & Pons, J. A. 2011, ApJL, 727, L51
Potekhin, A. Y., Pons, J. A., & Page, D. 2015, SSRv, 191, 239
Price-Whelan, A. M., Sipőcz, B. M., Günther, H. M., et al. 2018, AJ, 156, 123
Rankin, J. M. 1993, ApJ, 405, 285
Ransom, S. M., Eikenberry, S. S., & Middleditch, J. 2002, AJ, 124, 1788
Rea, N., Coti Zelati, F., Viganò, D., et al. 2020, ApJ, 894, 159
Remillard, R. A., Loewenstein, M., Steiner, J. F., et al. 2021, arXiv:2105.09901
Reynolds, M. T., Miller, J. M., Maitra, D., et al. 2013, ATel, 5200, 1
Ridnaia, A., Svinkin, D., Frederiks, D., et al. 2021, NatAs, 5, 372
Rodríguez Castillo, G. A., Israel, G. L., Esposito, P., et al. 2014, MNRAS, 441, 1305
Ruderman, M. A., & Sutherland, P. G. 1975, ApJ, 196, 51
Scargle, J. D., Norris, J. P., Jackson, B., & Chiang, J. 2013, ApJ, 764, 167
Shannon, R. M., & Johnston, S. 2013, MNRAS, 435, L29
Singh, S., & Roy, J. 2021, ATel, 14799, 1
Standish, E. M. 1998, JPL Planetary and Lunar Ephemerides, DE405/LE405, JPL Interoffice Memo 312.F-98-048, (Pasadena: NASA Jet Propulsion Laboratory)
Sturrock, P. A. 1971, ApJ, 164, 529
Tavani, M., Casentini, C., Ursi, A., et al. 2021, NatAs, 5, 401
Thompson, C., & Duncan, R. C. 1995, MNRAS, 275, 255
Thompson, C., & Duncan, R. C. 1996, ApJ, 473, 322
Tiengo, A., Vianello, G., Esposito, P., et al. 2010, ApJ, 710, 227
Wadiasingh, Z., Baring, M. G., Gonthier, P. L., & Harding, A. K. 2018, ApJ, 854, 98
Wadiasingh, Z., & Timokhin, A. 2019, ApJ, 879, 4
Wilms, J., Allen, A., & McCray, R. 2000, ApJ, 542, 914
Woods, P. M., Kaspi, V. M., Thompson, C., et al. 2004, ApJ, 605, 378
Woods, P. M., Kouveliotou, C., Finger, M. H., et al. 2007, ApJ, 654, 470
Woods, P. M., Kouveliotou, C., van Paradijs, J., et al. 1999, ApJL, 519, L139
Younes, G., Baring, M. G., Kouveliotou, C., et al. 2017a, ApJ, 851, 17
Younes, G., Kouveliotou, C., Jaodand, A., et al. 2017b, ApJ, 847, 85
Zhu, W., Kaspi, V. M., Dib, R., et al. 2008, ApJ, 686, 520